

1 **Longitudinal variations of positive dayside ionospheric storms related to**
2 **recurrent geomagnetic storms**

3
4 A. V. Dmitriev^{1,2}, C.-M. Huang¹, P. S. Brahmanandam^{1,3}, L. C. Chang¹, K.-T. Chen¹, L.-C. Tsai⁴

5 *¹Institute of Space Science, National Central University, Chung-Li, Taiwan*

6 *²Skobeltsyn Institute of Nuclear Physics Moscow State University, Moscow, Russia*

7 *³Dept. of ECE, K L University, Vaddeswaram, AP, India*

8 *⁴Center for Space and Remote Sensing Research, National Central University, Chung-Li, Taiwan*

9

10

11

12

13

14 Short title: RECURRENT IONOSPHERIC STORMS

15

16 _____

17 A. V. Dmitriev, Institute of Space Science, National Central University, Chung-Li, 320, Taiwan, also
18 at D.V. Skobeltsyn Institute of Nuclear Physics, Moscow State University, Russia (e-mail:
19 dalex@jupiter.ss.ncu.edu.tw)

20 C.-M. Huang, Institute of Space Science, National Central University, Chung-Li, 320, Taiwan (e-
21 mail: cmh@jupiter.ss.ncu.edu.tw)

22 P. S. Brahmanandam, Institute of Space Science, National Central University, Chung-Li, 320,
23 Taiwan (e-mail: anand.potula@gmail.com) also at Dept. of ECE, K L University, Vaddeswaram,
24 India.

25 L. C. Chang, Institute of Space Science, National Central University, Chung-Li, 320, Taiwan (e-mail:
26 loren@jupiter.ss.ncu.edu.tw)

27 K.-T. Chen, Institute of Space Science, National Central University, Chung-Li, 320, Taiwan (e-mail:
28 bestman8556@gmail.com)

29 L.-C. Tsai, Center for Space and Remote Sensing Research, National Central University, Chung-Li,
30 Taiwan (e-mail: lctsai@csrsr.ncu.edu.tw)

31

32 **Abstract**

33 We have performed an analysis of case events and statistics of positive ionospheric storms in the
34 dayside region of the equatorial ionization anomaly during recurrent geomagnetic storms (RGSs),
35 which dominate in geomagnetic and ionospheric conditions on the declining phase of solar activity in
36 2004 to 2008. It is shown that total electron content (TEC) has a tendency to minimize before the
37 beginning of RGSs and to peak 3 to 4 days after, i.e. on the RGS recovery phase produced by high-
38 intensity long-duration continuous auroral activity. The maximum of TEC coincides with the
39 maximum of solar wind velocity within high-speed solar wind streams. An analysis of electron
40 content vertical profiles, derived from two independent methods using ionosondes and
41 COSMIC/FORMOSAT-3 radio occultation, showed that in the maximum of an ionospheric storm on
42 [28 March 2008](#), the F2 layer thickens, NmF2 increases by ~50% and hmF2 elevates by a few tens of
43 kilometers. The response of positive ionospheric storms to solar, heliospheric and geomagnetic
44 drivers reveals a prominent longitudinal asymmetry. In the longitudinal range from -90° to 90° , the
45 solar illumination plays a major role, and in the range from 90° to -120° , the influence of
46 heliospheric and geomagnetic drivers becomes significant. The highest correlations of the TEC
47 enhancements with the heliospheric and geomagnetic drivers were found during December -
48 February period (r increased from ~ 0.3 to ~ 0.5). We speculate that the dynamics controlling this
49 might result from an effect of solar zenith angle, storm-time effects of thermospheric $\Sigma O/N_2$
50 enhancement, and penetrating electric fields of interplanetary and magnetospheric origin.

51

52

53 **Keywords:** Ionospheric storms, recurrent magnetic storms, corotating interaction regions, and high-
54 speed solar wind streams

55

56 **1. Introduction**

57 In recent years, a great deal of interest has been directed to recurrent geomagnetic storms (RGSs) and
58 their ionospheric and thermospheric effects [e.g. *Lei et al.*, 2008a;b;c; 2011; *Mlynczak et al.*, 2008;
59 *Thayer et al.*, 2008; *Denton et al.*, 2009; *Sojka et al.*, 2009; *Verkhoglyadova et al.*, 2011; *Liu et al.*,
60 2012a]. Comprehensive studies of the ionospheric day-to-day variability reveal that geomagnetic and
61 meteorological sources of the variations in the F2 layer ionization are comparable while the solar
62 radiation source is a minor contributor [*Forbes et al.*, 2000; *Rishbeth and Mendillo*, 2001]. The
63 regularity of interplanetary driving and thermospheric/ionospheric responses suggests a possibility to
64 develop a reliable 27-day prediction of ionospheric disturbances.

65 RGSs result from interaction of the magnetosphere with a complex interplanetary structure
66 consisting of high-speed streams (HSSs) of the solar wind preceded by corotating interaction regions
67 (CIR) formed between the fast and slow solar wind streams [*Burlaga and Lepping*, 1977; *Tsurutani*
68 *et al.*, 1995; 2011a]. During rising and declining phases of the solar cycle, RGSs occur almost every
69 7 to 13 days because of the draped heliospheric current sheet related to longitudinal distribution of
70 active regions and coronal holes on the Sun. The most dramatic geomagnetic response to the HSSs
71 are chains of consecutive substorms caused by the southward components of large-amplitude Alfvén
72 waves within the body of HSSs. This auroral activity has been named high-intensity long-duration
73 continuous AE activity (HILDCAAs) [*Tsurutani et al.*, 1995].

74 The RGSs are typically not very intense [*Richardson et al.*, 2006]. They peak at $Dst \sim -40$ nT but
75 have a prominent seasonal variation of ~ 40 nT which is ordered by the spring and fall equinoxes.
76 The substorm activity is generally most intense near the peak of HSS where the Alfvén wave
77 amplitudes are greatest, and it decreases with decreasing wave amplitudes and solar wind speed.
78 Hence, the RGSs have long-lasting main and recovery phases. The main phase is accompanied by
79 relatively high solar wind dynamic pressure and rapidly varying strong IMF B_z , associated with the
80 CIR. This phase is characterized by intense particle precipitation in the auroral region and from the

81 radiation belt to lower latitudes. The recovery phase is accompanied by HSSs and related
82 HILDCAAs, which contribute the fresh and sporadic injection of substorm energy leading to
83 unusually long storm recovery phases (up to ~10 days) as noted in *Dst*. This phase is also often
84 accompanied by relatively low solar wind density and weakened alternating IMF B_z .

85 There are a number of differences between the RGSs and CME-driven geomagnetic storms and their
86 ionospheric manifestations [Borovsky and Denton, 2006; Liu et al., 2012]. The main difference
87 consists in the penetration of the interplanetary electric field (IEF) in the magnetosphere. In contrast
88 to prompt (time scale of minutes) penetration for CME-driven storms [e.g. Guo et al., 2011], during
89 CIRs, the daytime ionospheric responses to IEF changes were found to occur within ~1 hour [Koga
90 et al., 2011]. Burns et al. [2012] suggested that while CIRs are substantial factor affecting the
91 thermosphere-ionosphere response, the level and duration of the continuing forcing during the HSSs
92 is also important. This continuing forcing leads to extended periods of storm effects in the
93 ionospheric electron content and enhanced neutral densities for many days after the end of the CIR
94 phase. Thus, although the magnitudes of RGSs are considerably smaller than those of CME-driven
95 storms, their cumulative effects on the thermosphere and ionosphere are comparable [e.g. Turner et
96 al., 2009].

97 A distinct global response of the ionosphere to RGSs was reported in a number of papers [e.g.
98 Denton et al., 2009; Ram et al., 2010; Pedatella et al., 2010; Pedatella and Forbes, 2011;
99 Verkhoglyadova et al., 2011; Liu et al., 2012a]. On average, the electron content in the low-latitude
100 ionosphere increases during the CIR-related main phase of RGSs. The virtual height of the F2 layer
101 peak (h_mF_2) on the dayside is found to increase by a few tens of km. During the long-lasting
102 recovery phase related to HSS, the electron content decreases but persists higher than the pre-storm
103 level. Ram et al. [2010] pointed out that the RGSs are characterized by a strong altitude and latitude
104 dependence of electron density perturbations, which can be explained by such physical processes as
105 photoionization-chemistry, particle precipitation, and dynamic and diffusion transport. The

106 disturbance dynamo electric field (DDEF) [*Blanc and Richmond, 1980; Huang et al., 2005*] is also
107 considered to be an important mechanism for driving the electrodynamic response of the dayside
108 ionosphere to recurrent geomagnetic activity related to high-speed solar wind streams [*Pedatella et*
109 *al., 2010; Pedatella and Forbes, 2011; Liu et al., 2012*].

110 Fast (within a few hours), global, and continuous ionospheric responses to RGSs were reported by a
111 number of authors [e.g. *Ram et al., 2010; Verkhoglyadova et al. 2011*]. The largest ionospheric
112 variations were found at low latitudes. It was concluded that CIRs/HSSs were external drivers for
113 both thermospheric and ionospheric phenomena. A global thermospheric heating was revealed
114 during RGSs. For instance, *Sojka et al. [2009]* found a significant increase of the ion temperature in
115 the high-latitude ionosphere during CIR intervals. Prominent increases of low-latitude thermospheric
116 density and $\Sigma O/N_2$ during RGSs were also found in a number of studies [*Lei et al., 2008a; 2011;*
117 *Crowley et al., 2008; Burke et al., 2010; Liu et al., 2012b*]. *Burke et al. [2010]* have shown that a
118 model used to estimate exospheric temperature changes during large CME-driven storms
119 overpredicts the thermospheric heating during RGSs. However, large-amplitude Alfvén waves in the
120 interiors of HSSs generate regularly observed increases in the exospheric temperature. *Deng et al.*
121 *[2011]* concluded that the energy transfer process into the upper atmosphere associated with HSSs is
122 a combination of Joule heating and particle precipitation at high latitudes, while Joule heating plays a
123 dominant role.

124 An important manifestation of efficient heliospheric-magnetospheric-ionospheric-thermospheric
125 coupling occurring during RGSs is a 9-day periodicity in variations of the ionospheric and
126 thermospheric parameters [*Crowley et al., 2008; Lei et al., 2008a;b;c; Mlynczak et al., 2008; Thayer*
127 *et al., 2008; Chang et al., 2009; Pedatella et al., 2010; Ram et al., 2010; Liu et al., 2010a; 2012a*]. On
128 average, at low-middle latitudes, the 9-day oscillations in thermospheric density, temperature and
129 such ionospheric parameters as electron density in the maximum of F2 layer (NmF2), hmF2 and the
130 thickness of F2 layer (HT) are in phase with those in geomagnetic activity.

131 However, in the equatorial anomaly region, the ionosphere shows more complicated day-to-day
132 variability. *Wang et al.* [2011] found that low-latitude stations, located at different longitudes,
133 detected ionospheric variations with different periodicities of 11 and 16 – 21 days, though the 9-day
134 periodicity was dominant. The difference indicates a longitudinal inhomogeneity in the ionospheric
135 day-to-day variability related to geomagnetic variations as well as to other sources.

136 It can be seen that the pattern of the ionospheric response to the recurrent geomagnetic activity is
137 very complex and quite different from the well-developed model of “standard” storms proposed by
138 *Fuller-Rowell et al.* [1994]. However, the cumulative ionospheric effect of RGSs and CME-driven
139 storms can be comparable. The complexity of temporal and spatial dynamics of the ionosphere
140 during RGSs results from strong and fast variations of external drivers such as IEF and solar wind
141 dynamic pressure, together with intense particle precipitations in the magnetosphere that results in
142 strong variations of prompt penetration electric field (PPEF), disturbance dynamo electric field
143 (DDEF), thermospheric density and chemical composition [e.g. *Wang et al.*, 2011; *Burns et al.*,
144 2012; *Liu et al.*, 2012a]. Past studies on RGS-related disturbances in the thermosphere and
145 ionosphere focused mainly on the zonally symmetric component that assumes an identical response
146 at all longitudes. In addition, statistical studies of RGS-related ionospheric/thermospheric
147 disturbances did not distinguish between the CIR-related main phase and HSS-related maximum and
148 recovery phase of RGSs.

149 In the present paper, we investigate longitudinal variations of the ionization enhancements in the
150 low-latitude dayside ionosphere (so-called positive ionospheric storms) during different phases of
151 RGSs. The organization of present paper is as follows: Statistical study of positive ionospheric
152 storms is presented in Section 2. Vertical profiles of enhanced electron content are investigated in
153 Section 3. The results are discussed in Section 4. The conclusions are given in Section 5.

154

155 **2. Positive ionospheric storms**

156
157 We study positive ionospheric storms that occurred from 2004 to 2008 during the declining phase of
158 solar activity. As shown in Figure 1, this interval is characterized by relatively low levels of the solar
159 radiation represented by the solar radio flux with wavelength of 10.7 cm (F10.7 index). The F10.7
160 index can be considered as a proxy of the solar radiation controlling the dayside ionospheric
161 ionization [Ozguç *et al.*, 2008; A *et al.*, 2012]. During declining and minimum phases as well as
162 during rising phases of solar cycle, the heliospheric and geomagnetic conditions are dominated,
163 respectively, by CIR/HSSs and by RGSs, whose amplitude, measured as a minimum *Dst* variation,
164 does not usually exceed several tens of nT [e.g. Bothmer *et al.*, 2004]. We do not consider the year of
165 2009 when a deep minimum occurred in solar, heliospheric, geomagnetic and
166 ionospheric/thermospheric activity [Tsurutani *et al.*, 2011b; Verkhoglyadova *et al.*, 2013].

167

168 **2.1. Global ionospheric maps**

169 The long time scales of RGSs make it possible to study ionospheric effects of these storms with 2-
170 hour resolution. This time resolution is widely used for a global ionosphere mapping such 2-D global
171 ionospheric maps (GIMs) of vertical total electron content (VTEC) derived from the global
172 positioning system (GPS) network [Rebischung *et al.*, 2012; <http://aiuws.unibe.ch/ionosphere/>].
173 GIMs are generated using data acquired from about 200 ground-based receivers of the radio-signals
174 from GPS and GLONASS satellite constellations and analyzed by the International Global
175 Navigation Satellite Systems Service (IGS) and other institutions
176 [<http://igsceb.jpl.nasa.gov/network/refframe.html>]. The reliability of GIMs was investigated in a
177 number of studies [e.g. Hernandez-Pajares *et al.*, 2009; Jee *et al.*, 2010]. It was shown that on the
178 whole, GIMs were largely able to reproduce the spatial and temporal variations of the global
179 ionosphere as well as annual and semiannual variations and solar cycle variations.

180 Table 1 shows number of IGS receivers used for construction of GIM at low- to mid-latitudes in
181 different longitudinal ranges. Above the Pacific Ocean (longitudes from 150° to 180° and from –
182 180° to -120°), the number of receivers is less than that above continents. However, each
183 longitudinal range is represented by at least 4 receivers located in both Southern and Northern
184 hemispheres at low- to mid-latitudes that allows for measuring a region of the equatorial ionization
185 anomaly (EIA).

186 An example of GIMs is shown in Figure 2. The maps, constructed during a recurrent magnetic storm
187 on 27 and 29 March 2008, are compared with a quiet day on 25 March 2008. Solar, heliospheric and
188 geomagnetic conditions during the storm are presented in Figure 3. Namely, March 27 and 29
189 correspond, respectively, to the maximum and recovery phase of the storm. The residual VTEC
190 reveals prominent positive ionospheric storms, with enhancements up to >20 TECU occurring at low
191 latitudes in the postnoon and evening sectors in Indochina, Pacific, and American regions. It is
192 important to note that the largest enhancements of VTEC are observed in the crest of EIA. Hence, it
193 is possible to analyze the positive ionospheric storms by studying the maximum VTEC in the EIA
194 region.

195 The 2-hour time step of GIMs is equivalent to a 30° step in longitude. That allows for dividing the
196 map onto 12 longitudinal ranges: from -180° to -150°, from -150° to -120° ... from 150° to 180°. We
197 can, thus, construct a portion of GIM every two hours and for each longitudinal range. Spatial VTEC
198 distribution varies with local time and, hence, with UT such that higher (lower) VTEC appear on the
199 dayside (nightside). For each day and for each longitudinal range, we determine a daily maximum
200 VTEC (maxVTEC).

201 Examples of variations of VTEC distributions and maxVTEC within 27-day intervals in various
202 longitudinal ranges are presented in Figures 3 and 4, respectively, during spring equinox (from 20
203 March to 15 April 2008, a part of Whole Heliospheric Interval [e.g. *Verkhoglyadova et al.*, 2011])
204 and near the winter solstice (from 1 January to 3 February 2007). The interval of 27 days is

205 approximately equal to a period of solar rotation in the Earth's frame that is a prime source of the
206 recurrent variations. Figures also show time profiles of daily solar radiation (F10.7), and 1-min data
207 of solar wind velocity (V_{sw}), density (D), IMF B_z in GSM coordinates, and 1-hour geomagnetic
208 indices AE , Dst and 3-hour Kp . Solar wind parameters were acquired from ACE and Wind upstream
209 monitors. The Wind monitor was used when the ACE data was poor due to numerous data gaps. For
210 the days when neither ACE nor Wind data were available, such as 26 March 2008 in Figure 3, we
211 eliminated the solar wind data from consideration.

212 During 27-day periods, we observe 2 or 3 intervals of co-rotating CIR-HSS structures, characterized
213 by high solar wind speeds of >400 km/s. The total duration of these structures varies from 4 to 10
214 days. The co-rotating streams result in recurrent geomagnetic storms of similar duration and
215 repeating time. The onset of RGS is determined as an abrupt increase of geomagnetic indices AE , Kp
216 and Dst . The increase results from magnification of southward IMF in compressed solar wind of the
217 CIR region. The time interval between the onsets varies from 7 to 13 days. The storms are
218 characterized by a high level of the auroral activity (large AE index) as well as by global
219 geomagnetic disturbances revealed in enhanced Kp and Dst indices (with minimum Dst of about -40
220 nT).

221 As one can see in Figure 3, maxVTEC occurs mainly in the crest of the EIA. On March 24 – 25,
222 maxVTEC increased with the solar radiation index F10.7. The increase was stronger in the
223 longitudinal range from -120° to -90° and weaker in the ranges from 90° to 120° and from -30° to
224 0° . At the same time, maxVTEC also enhanced during recurrent magnetic storms that occurred on
225 March 26 – April 2 (8-day duration) and April 4 – 14 (11-day duration). Note that the former storm
226 overlapped with F10.7-related increase of VTEC. The VTEC enhancements were mostly prominent
227 in the longitudinal range from -120° to -90° . It is interesting to note that maxVTEC peaks several
228 days after the onset of RGSs. Namely, the maximum values of maxVTEC occurred on March 27 –
229 28 (2 – 3 days after the RGS onset) and on April 5 – 8 (1 – 4 days after the RGS onset). In the range

230 from 90° to 120° , an additional prominent maximum of maxVTEC occurred on April 10, i.e. 6 days
231 after the RGS onset.

232 It is interesting to note that the CIR-related onsets of RGS (March 26 – 27 and April 4 – 5) were
233 accompanied by suppressions of maxVTEC. Most prominent suppressions were observed in the
234 longitudinal range from -120° to -90° . At ~ 22 UT on April 4, the suppression was accompanied by
235 the northward IMF. On the other hand, another prominent suppression can be found at ~ 14 UT on
236 April 4 in the longitudinal range from -30° to 0° . At that time, the IMF was southward and large.

237 During the late recovery phase of RGSs, maxVTEC was decreasing at all longitudes. The decrease
238 was not gradual but sustained a day-to-day variability with local minima and maxima occurred at
239 different longitudes during different days. Very low maxVTEC in the EIA region was observed at all
240 longitudes during a few days between the recurrent storms (March 24, April 2-3 and 14). Those days
241 are characterized not only by very low geomagnetic activity but also by quiet interplanetary
242 conditions characterized by low solar wind speed and weak IMF B_z variations.

243 A similar pattern of the VTEC dynamics can be found during winter solstice (Figure 4). Note that
244 maxVTEC occurs mainly in the southern crest of the EIA that corresponds to better illumination of
245 the Southern hemisphere. From January 8 to February 4, we distinguish two RGSs: January 14 – 26
246 (13-day duration) and January 29 – February 4 (7-day duration). The former (latter) storm was
247 accompanied by a decrease (increase) of $F_{10.7}$. Quiet days in the ionosphere can be identified via
248 low maxVTEC on January 13 and 27-28. They were characterized rather by low solar wind speed
249 and weak IMF B_z variations while geomagnetic activity was slightly disturbed.

250 Suppressions of maxVTEC can be seen during CIR intervals on January 14-15 in longitudinal ranges
251 from 0° to 30° and from 120° to 150° and on January 30 in all longitudinal ranges. Note that on
252 January 14, northward IMF accompanied the suppression in the range from 0° to 30° while the
253 suppression in the range from 120° to 150° occurred on January 15 under southward IMF. January

254 30 was characterized by highly variable IMF. Hence, it seems the suppression is driven not only by
255 the IMF orientation.

256 Enhancements of maxVTEC are observed at all longitudes on January 16 – 17 (2 – 3 days after the
257 RGS onset) and on January 31 – February 2 (2 - 4 days after the RGS onset). It is important to point
258 out that the RGS-driven variation of maxVTEC is comparable with and, thus, can be hidden by the
259 variation related to $F10.7$. Therefore, we have to separate these two drivers carefully and such efforts
260 have been made in this research.

261 Hence, the maximal VTEC occurs usually 2 to 4 days after the RGS onset and sometimes even on
262 the late stage of the recovery phase of RGSs. Most prominent enhancements of maxVTEC were
263 rather related to HSSs. The amplitude of maxVTEC variations during RGSs can be estimated as
264 being in the range of tens of TECU. In addition, we have found a difference of the order of ~ 10
265 TECU in the ionospheric response to RGSs in different longitudinal sectors. Namely, the variations
266 of maxVTEC in the longitudinal ranges from -150° to -90° and from 90° to 150° are much stronger
267 than those in the range from -30° to 30° .

268 It is important to point out that the ionosphere and geomagnetic activity is disturbed by RGSs during
269 most of time. There are only a few quiet days in the ionosphere per 27-day solar rotation period.
270 Those days are characterized by both low geomagnetic activity and quiet solar wind. Similar patterns
271 can be found for all other 27-day intervals in 2004 – 2008. Therefore, RGS-related ionospheric
272 effects contribute a significant portion of the statistics.

273

274 **2.2. Superposed epoch analysis of RGS-related maxVTEC variations**

275 In order to study ionospheric effects of recurrent geomagnetic storms, we consider only weak and
276 moderate magnetic storms with $Dst > -70$ nT. As one can see in Figure 1, strong magnetic storms
277 with peak $Dst < -70$ nT produce only a small portion of the statistics. Superposed epoch analysis is
278 based on 185 RGSs occurred from 2004 to 2008. The time is calculated from the onset of RMS (day

279 = 0). The negative and positive time corresponds to periods, respectively, before and after the storm
280 onset.

281 A distribution of local time of RGS onsets is presented in Figure 5. We distinguish four local time
282 sectors: midnight (LT = 21 – 3), morning (LT = 3 – 9), noon (LT = 9 – 15), and evening (LT = 15 –
283 21). It can be clearly seen that the occurrence probability of onsets does not practically depend on the
284 local time. An excess (deficiency) of the onsets in the noon (evening) sectors does not exceed 2
285 standard errors. Hence, longitudinal differences in the ionospheric response (if any) should weakly
286 depend on the differences in local time of RGS onsets.

287 The superposed epoch analysis is performed for daily values. Note that for each storm, the time starts
288 (day = 0) from the onset such that the analyzed days are different from the calendar days. Within 10-
289 day time intervals starting 2 days before the onset and lasting 8 days after (if possible), we calculate
290 for each day a minimum of Dst and Bz , maximum of Vsw , D , Kp , and AE as well as maxVTEC in
291 various longitudinal sectors. Note that RGSs with duration less than 8 days contribute to the statistics
292 of the first few days only.

293 Figure 6 demonstrates examples of the superposed epoch analysis applied for minimum Dst and
294 maxVTEC in longitudinal ranges from 0° to 30° and from 120° to 150° . These ranges are well
295 covered by IGS receivers (see Table 1). For comparative analysis of maxVTEC variations, we
296 subtract mean values of maxVTEC calculated upon all statistics in different longitudinal ranges (see
297 Figure 7) such that maxVTEC varies around zero. Recurrent storms are characterized by a prominent
298 day-to-day geomagnetic and ionospheric variability, which is exhibited by jumps of Dst and
299 maxVTEC. This variability is clearly seen in Figures 3 and 4. Variations of maxVTEC in the
300 longitudinal range from 120° to 150° exceed 10 TECU quite often while variations in the range from
301 0° to 30° are mainly below 10 TECU. Variations of median maxVTEC, calculated upon all RGSs,
302 have amplitudes, respectively, of 3.2 and 2.4 TECU that corresponds to ~30% difference. Note that
303 this difference between medians is significant because it results from large statistics of 185 RGSs.

304 In Figure 6, variations of median Dst and median maxVTEC exhibit a certain temporal pattern.
305 Namely, largest values of Dst (~ -10 nT) are revealed before and on the first day of RGSs (day = -2
306 to 0). The median Dst reaches minimum of about -27 nT on the second day of the storm (day = 1)
307 and then Dst restores gradually. During RGSs, day-to-day variability of Dst is produced by two
308 competitive drivers: solar wind pressure Pd and IMF Bz . Positive variations in Dst are produced by
309 northward turning IMF ($Bz > 0$) as well as by enhancements in the Pd (solar wind density and/or
310 velocity) resulting in magnetospheric compression and intensification of Chapman-Ferraro current at
311 the magnetopause [e.g. *O'Brien and McPherron, 2002*]. Increases of southward IMF ($Bz < 0$) lead to
312 negative Dst variations. It seems that the small negative $Dst \sim -10$ nT during the RGS onset results
313 from high Pd whose geomagnetic effect is stronger than the effect of southward IMF. The latter can
314 be strong but its duration is usually short that does not allow large negative Dst variation.

315 The variation of median maxVTEC follows the Dst variation only partially. A prominent decrease of
316 median maxVTEC is observed right before the onset (day = -1). Then maxVTEC increases gradually
317 during 3 days up to the maximum values (day = 2) and decreases during the rest of time. Note that
318 the maximum of median maxVTEC occurs one day after the minimum of Dst that might be related to
319 HILDCAAs. The onset of RGS can be accompanied by both suppressed and enhanced maxVTEC. In
320 the range from 0° to 30° , negative variations occur more often such that the variation of median
321 maxVTEC at day = 0 is negative (-0.3 TECU).

322 Figure 7 shows longitudinal changes in maxVTEC variations. The amplitude of variations (a
323 difference between maximum and minimum) of the median maxVTEC increases by ~ 2 times from \sim
324 2 TECU in the longitudinal range $-60^\circ - 120^\circ$ to ~ 4 TECU in the range $120^\circ - -60^\circ$ (i.e. from 120° to
325 180° and from -180° to -60°). This difference can be considered to be significant because it was
326 obtained from large statistics of 185 RGSs. The variations of median maxVTEC at day = 0 are
327 negative practically at all longitudes that indicates a predominant suppression of maxVTEC during
328 the RGS onsets.

329 For each longitude range, we also estimated an average enhancement of maxVTEC by averaging the
330 maximal values of maxVTEC observed during each RGS. The average enhancement varies with
331 longitude substantially (~60%) from ~5 TECU in the longitudinal range from -60° to 60° to ~8
332 TECU in the range from longitudes from 60° to -60° . Hence, we can conclude that the longitudinal
333 regions from -60° to 60° and from 120° to -60° are characterized, respectively, by lowest and highest
334 variability of maxVTEC. Note that both regions contain several longitudinal ranges with good
335 coverage by IGS receivers that support the validity of our results.

336 We have to point out that the present pattern of longitudinal variations in maxVTEC is quite different
337 from the pattern of LT variation in RGS onsets presented in Figure 5. Hence, the weak LT variation
338 of RGSs has a minor contribution to the observed longitudinal variation of maxVTEC, which would
339 be driven by other significant effects.

340 In Figure 7 we also present mean values of maxVTEC calculated for each longitudinal range as
341 average of maxVTEC upon whole statistics, including quiet days and 185 RGSs. The mean
342 maxVTEC demonstrates a prominent longitudinal variability of ~15% with minimum around 41
343 TECU in the longitudinal range from -60° to 60° and maximum around 47 TECU in the ranges
344 from -180° to -120° and from 90° to 120° . It is important to point out that similar longitudinal
345 variation with amplitude of a few tens of percent was revealed by *Liu et al.* [2011] on the base of
346 comprehensive statistical analysis of electron content determined by radio-occultation technique in
347 COSMIC/FORMOSAT-3 space experiment, for which the quality of ionospheric data is
348 longitudinally independent. It was reported that in the postnoon sector, the average low-latitude
349 NmF2 reached maximal values in two longitudinal ranges: from 90° to 150° and from -180° to -60° ,
350 i.e. practically in the same ranges as those for the mean maxVTEC. The good correspondence of the
351 results, obtained by two different ionospheric techniques, is a strong proof of the validity of the
352 techniques used. Hence, our results about longitudinal variations of VTEC obtained from the GIM
353 technique are robust.

354 Figure 8 shows RGS-related temporal dynamics of the median maxVTEC in comparison with
355 average variations of the solar wind and geomagnetic parameters. Note that the average variation of
356 the solar radiation index F10.7 (not shown) is negligibly weak during RGSs and, thus, it does not
357 affect the average ionospheric variations. In contrast, the solar wind and geomagnetic parameters
358 exhibit prominent average variations during RGSs.

359 Before RGS (day = -2 and -1), the solar wind velocity and density are low and $B_z \sim 0$ that promote a
360 quiet geomagnetic activity and low maxVTEC. The beginning of RGS (day = 0) is caused by a CIR
361 region, in which the solar wind density and negative B_z reach maximum values that result in
362 intensification of geomagnetic activity and growth of K_p and AE indices. The increase of solar wind
363 density and velocity prevents a sharp decrease of the Dst index. On the second day (day = 1), B_z
364 persists negative and high while the solar wind velocity increases but the density decreases that
365 results in generation of storm maximum with peak values of the geomagnetic indices. On average,
366 K_p and AE demonstrate quite well anti-correlation with the Dst index.

367 It is interesting to note that the solar wind velocity peaks on the third day of RGS (day = 2), i.e. on
368 the next day after the RGS maximum. At that time, the southward IMF decreases slightly, the solar
369 wind density approaches to its nominal value of $\sim 5 \text{ cm}^{-3}$ and the geomagnetic activity is diminishing.
370 At the same day, the median maxVTEC reaches maximum in practically all the longitudinal ranges.
371 In the range from 150° to 180° , the maximum of median maxVTEC is observed even on the fourth
372 day of RGS (day = 3). On average, the maxVTEC variation correlates better with the solar wind
373 velocity than with the geomagnetic indices. The minimal values of median maxVTEC are observed
374 right before the onset and in the late recovery phase of RGSs. Such dynamics of maxVTEC allow us
375 to introduce so-called “recurrent ionospheric storms” related rather to CIR/HSS solar wind structures
376 than to RGS alone.

377

378 **2.3. Correlations with solar, heliospheric and geomagnetic parameters**

379 *Lei et al.* [2008c] found high correlation between variations in the thermosphere and solar wind and
380 geomagnetic parameters. It is reasonable to expect a high correlation for the ionospheric variations.
381 As a first step, we calculate correlation of daily maxVTEC in 2004 to 2008 with solar wind–
382 magnetosphere coupling functions such as Newell’s merging $V^{4/3}B^{2/3}\sin^{8/3}(\theta_c/2)$ and viscous
383 $D^{1/2}V^2$ functions [Newell et al., 2008] and Kuznetsov’s merging $V\sqrt{B-B_z}$ and viscous $DV^{3.5}$
384 functions [Kuznetsov et al., 1993]. Here V , D , B , B_z , and θ_c are, respectively, solar wind velocity,
385 density, IMF strength, Z-component and clock angle. We have found poor correlations: 0.17 (partial
386 correlation coefficients, respectively, 0.07 and 0.16) for the Newell’s coupling function and 0.25
387 (0.24 and 0.12, respectively) for the Kuznetsov’s coupling function. Hence, the low-latitude
388 ionosphere would be driven by other parameters.

389 For further analysis, we represent maxVTEC as a linear function F :

390

$$391 \quad F = a_0 + a_{\cos} \cos\alpha + a_{1F10.7}F10.7 + a_{2F10.7}F10.7^2 + a_{V_{sw}}V_{sw} + a_D D + a_{B_z}B_z + a_{AE}AE + a_{Kp}Kp + a_{Dst}Dst$$

392 (1)

393

394 Here we take into account a quadratic dependence of VTEC from F10.7, as a much more accurate
395 approximation than a simple linear dependence [e.g. *Liu and Chen*, 2009]. In order to describe a
396 dependence on the ionosphere illumination by sunlight during various seasons, we introduce a
397 subsidiary parameter, so-called annual angle α :

398

$$399 \quad \alpha = \pi * ((DOY - DOY1)/(DOY2 - DOY1)), (2)$$

400

401 where DOY is a day of year, DOY1 and DOY2 are DOYs of June 22 and December 12, respectively.
402 The cosine of the annual angle ($\cos\alpha$) is close to 0 during equinoxes and approaches to 1 (-1) during

403 northern summer (winter) solstice. The annual angle can be considered as an equivalent of the solar
404 zenith angle relative to the geographic equator at the noon meridian.

405 For the heliospheric parameters including V_{sw} , D , B_z , we use maximum values determined within
406 the 3 hours before the maxVTEC occurrence. This time includes ~1 hour for the solar wind
407 propagation from the upstream monitor plus 2 hours of the time resolution. For the geomagnetic
408 parameters Kp and Dst , we use, respectively, maximal and minimal values determined within 9 hours.
409 We also use the maximum of the AE index within 6 hours before the maxVTEC occurrence. The 9-
410 hour interval includes 2 hours of the time resolution plus ~7 hours, which we assume to be required
411 for the development of the ionospheric response to the magnetospheric perturbations. The 6-hour
412 interval for the AE index is based on an assumption that equatorward neutral winds might require up
413 to ~4 hours to propagate from the auroral region to the equator. The free coefficients are calculated
414 for each longitudinal range by a linear regression method applied for the time profiles of maxVTEC
415 and driving parameters (see Eq. 1) during practically the whole time interval from 2004 to 2008.
416 Hence, the statistics include more than 1700 sets of parameter values during both RGSs and quiet
417 days for 12 longitudinal ranges.

418 Figure 9 shows longitudinal variation of the correlation between maxVTEC and various parameters.
419 We have found that maxVTEC correlates poorly with B_z and D (not shown). Hence, we exclude
420 these parameters from further consideration. In addition, the geomagnetic indices Kp and Dst inter-
421 correlate quite well. However, the 1-hour Dst index demonstrates higher correlation with maxVTEC
422 than the 3-hour Kp index (not shown). Hence, we also exclude the Kp index from further
423 consideration. Finally we analyze the following linear combination of 6 parameters:

424

$$425 \quad F_6 = a_0 + F_2 + a_{\cos} \cos\alpha + a_{V_{sw}} V_{sw} + a_{AE} AE + a_{Dst} Dst \quad (3a)$$

$$426 \quad F_2 = a_{0F107} + a_{1F107} F10.7 + a_{2F107} F10.7^2 \quad (3b)$$

427

428 As one can see in Figure 9a, the correlation of maxVTEC with other parameters varies significantly
429 (within 3 stat-errors) with longitude. Lowest correlations can be seen in the longitudinal ranges
430 from -120° to -60° and from 60° to 120° . Highest correlations of $r \sim 0.8$ and $r \sim 0.75$ can be found,
431 respectively, with F_6 and F_2 in the longitudinal range from -60° to 60° . In the range from 150° to -
432 120° (i.e. from 150° to 180° and from -180° to -120°), the correlation with F_6 is also high ($r \sim 0.8$)
433 while the correlation with F_2 is lower ($r \sim 0.7$). It seems the dynamics of maxVTEC in the
434 longitudinal range from 150° to -90° is controlled not only by solar radiation but other parameters
435 that become important there.

436 A relatively high correlation of ~ 0.3 can be found between maxVTEC and maximal *AE* index in the
437 latitudinal range from -150° to -60° (see Figure 9b). The maximal solar wind velocity has quite low
438 correlation with maxVTEC but this correlation exceeds 0.15 in the longitudinal range from 150° to -
439 90° . More prominent increases in correlation can be found for the *Dst* index (Figure 9c). In the range
440 from 150° to -30° , the anti-correlation of negative *Dst* with positive maxVTEC exceeds 0.35. Hence,
441 in the longitudinal range from 120° to -90° the effect of heliospheric and geomagnetic parameters to
442 the ionosphere is more ordered that produces an additional contribution to the correlation with
443 maxVTEC. It is interesting to point out an effect of annual angle (Figure 9c), which exhibits a sharp
444 increase of anti-correlation ($r \sim 0.3$) in the latitudinal range from 120° to -120° , in comparison with
445 poor anti-correlation ($r < 0.2$) at other longitudes. We will discuss this effect later.

446 Figures 10 and 11 show seasonal variations in the correlation. Highest correlations of maxVTEC
447 with F_6 (all the parameters) can be found at longitudes from -60° to 60° during summer (June –
448 August), winter (December – February) and autumn (September – November) seasons (see Figure
449 10a). It seems that the correlation during spring (winter) is lower (higher) than that during other
450 seasons. In Figure 10b one can clearly see a statistically significant decrease of the correlation with
451 F_2 (function of $F_{10.7}$) during the spring season. Perhaps, the decrease of the maxVTEC correlation
452 with F_6 results from the dependence on solar radiation.

453 In Figure 11a, one can see that the spring season is also characterized by relatively high anti-
454 correlation between maxVTEC and the annual angle in the range of longitudes from 120° to -90° . A
455 similar tendency but with lower correlation can be found for the autumn season. Hence, the
456 enhancement of anti-correlation between maxVTEC and $\cos\alpha$, demonstrated in Figure 9c, is related
457 to the equinoxes. Another interesting feature in Figure 11a is a relatively high correlation between
458 maxVTEC and $\cos\alpha$ in the longitudinal range from -90° to 90° during winter. Note that maxVTEC
459 has highest correlations with the solar radiation index $F10.7$ (see Figure 9a) in almost the same range
460 (from -60° to 60°).

461 It is important to point out that higher winter (December to February) correlation is also revealed for
462 heliospheric and geomagnetic parameters (see Figure 11). In general, the longitudinal variations of
463 the correlations during different seasons have similar patterns as shown in Figure 9. Namely, the
464 correlations increase in the longitudinal range from 120° to -90° . The highest correlations are found
465 during the period from December to February such that the correlation approaches and exceeds 0.5
466 and 0.3 for geomagnetic indices and for V_{sw} , respectively. Hence, the ionospheric storms correlate
467 better with RGSs around winter solstice.

468

469 **3. Height profiles of disturbed electron content**

470

471 A comprehensive statistical analysis of the ionospheric response to RGSs was performed on the base
472 of COSMIC/FORMOSAT-3 space-borne data by *Ram et al.* [2010]. They dealt with zonal average
473 electron density and did not distinguish between different phases of RGS related, respectively, to
474 CIR and HSS. In order to study physical mechanisms of generation of positive ionospheric storms at
475 different longitudes during RGSs, however, we consider vertical profiles of the electron density (EC)
476 measured by ionosondes and retrieved from COSMIC/FORMOSAT-3 observations during the HSS-
477 related maximum of RGS and ionospheric storm on 25 March 2008.

478 We have used the advanced Digital Ionosonde (Digisonde-4D or DPS-4D) database obtained from
479 Kwajalein and from Jicamarca stations. The height profiles of EC were ‘True Height Profiles’ which
480 are obtained by the ARTIST-5 (Automatic Real-Time Ionogram Scaler with True Height) software.
481 ARTIST-5 software calculates automatically the topside profile based on the bottomside profile of
482 the ionogram by using appropriate extrapolation techniques, so that full profiles of EC can be
483 obtained unambiguously. Further details on ARTIST-5 algorithms can be obtained from *Galkin et al.*
484 [2008].

485 The COSMIC/FORMOSAT-3 constellation of six low-orbit satellites produces a sounding of the
486 ionosphere using the radio occultation (RO) technique, which makes use of radio signals transmitted
487 by the GPS satellites [*Hajj et al.*, 2000]. Usually over 2500 soundings per day provide EC height
488 profiles at altitudes from the Earth surface to the orbital altitude at ~800 km over ocean and land. A
489 3-D EC distribution can thus be deduced through relaxation using red-black smoothing on numerous
490 EC height profiles [see *Tsai et al.*, 2006]. This 3-D EC image is used as an initial guess to start the
491 iterative Multiplicative Algebraic Reconstruction Technique (MART) algorithm, and 3-D
492 tomography of the EC is then produced with a time step of 2 hours around whole globe with spatial
493 grid of 5° in longitude, 1° in latitude, and 5 km in height. Such tomographic investigations give
494 valuable information in a wide region, without use of models.

495 Figure 12 shows the height profile of EC in the Pacific region at ~ 2 UT during the quiet day of 25
496 March 2008 and in the maximum of RGS-related ionospheric storm on 28 March 2008. The height
497 profiles of EC were measured by an ionosonde located at Kwajalein (9°N, 167°E). As one can
498 clearly see in Figure 12a, the NmF2 increased significantly (more than 50%), the F2 layer is
499 thickening and the hmF2 elevated up to ~ 50 km from the height of ~250 km to ~300 km. From
500 COSMIC/FORMOSAT-3 RO data, we reconstructed a meridional cut of EC in the range from 165°
501 to 170° corresponding to ~13 LT (see Figure 12b). In this cut, the maximum of F2 layer was located
502 in the southern crest of EIA. During the storm maximum, a total EC (TEC), integrated through all

503 heights at latitude of the maximum (lat $\sim 5^\circ$), increased up to ~ 18 TECU in comparison with ~ 13
504 TECU during the quiet day, i.e. by $\sim 50\%$. In addition, the hmF2 in the southern crest increased by a
505 few tens of km and the thickness of F2 layer also increased.

506 Figure 13 shows an example of RGS-related dynamics of the EC height profiles in the South
507 American region. According to ionosonde measurements at Jicamarca (12°S , 77°W), the NmF2 in
508 the postnoon sector (22UT and 17LT) increased significantly and elevated from ~ 300 km height on
509 the quiet day of 25 March 2008 to ~ 350 km during the storm on 28 March 2008 (see Figure 13a).
510 Note that hmF2 in the American region is ~ 50 km higher than that in the Pacific region. The
511 reconstruction of EC meridional cut from COSMIC/FORMOSAT-3 RO data in the range from -80°
512 to -75° (Figure 13b) showed that during the storm, the NmF2 moved from the quiet-day location in
513 the northern crest to the storm-time southern crest. The storm-time F2 layer was much thicker than
514 that at the quiet day. The TEC increased by $\sim 50\%$ in the whole EIA region from quiet values of 15 –
515 18 TECU to storm-time values of 20 - 24 TECU. At the latitude of maximum (lat $\sim -14^\circ$), the TEC
516 increased from ~ 15 TECU to ~ 22 TECU and the hmF2 elevated from ~ 290 km to ~ 310 km. Note
517 that in the northern crest, the hmF2 increased from ~ 330 km to ~ 340 km.

518 Considering Figures 12 and 13, we can also find that the topology of EIA is not changed very much
519 in the storm maximum. In particular, the latitude of the crests remains almost constant. Using results
520 by *Balan and Bailey* [1995], we estimated that ~ 50 km increase in hmF2 should result in a poleward
521 displacement of the crest regions by about a few degrees, which was hard to distinguish using $1^\circ \times 5^\circ$
522 angular resolution. Hence, in the maximum of RGS-related ionospheric storm [on 28 March 2008](#), the
523 EIA is intensified: the F2 layer is thickening, the NmF2 increases by $\sim 50\%$ and the hmF2 elevates by
524 a few tens of kilometers.

525

526 **4. Discussion**

527

528 From analysis of global ionospheric maps during declining phase of the 23-rd solar cycle (2004 –
529 2008), we have found that recurrent geomagnetic storms result in positive ionospheric storms at low-
530 latitudes on the dayside. The storms are revealed as prominent enhancements of VTEC in the EIA
531 region. We have also found that the amplitude of positive ionospheric storms varies substantially
532 with longitude. The longitudinal variations in the RGS-driven ionosphere are difficult to explain by
533 the effects typical for CME-driven storms such as an effect of “storm start time” [Fuller-Rowell *et al.*,
534 1994]. As one can see in Figures 5, the RGSs onsets are practically equally probable at different UT.
535 Moreover, RGSs last for several days and largest enhancements of VTEC occur ~2 days after the
536 onset and ~1 day after the storm maximum (see Figure 8) such that the ionosphere losses information
537 not only about the onset but also about the main phase of a storm. In contrast to CME-driven storms,
538 an RGS is generated by two geoeffective solar wind structures: CIR and HSS. The onset and main
539 phase of RGS are related to CIR. The prolonged maximum and recovery phase are related to HSS.
540 In the beginning of RGS, VTEC in the crest regions of EIA does not exhibit any prominent
541 enhancement and even has a tendency to be suppressed (see Figure 3, 4, 7 and 8). Such behavior can
542 be caused by an increase of recombination rate. *Verkhoglyadova et al.* [2011] reported an excess of
543 thermospheric heating at low to high latitudes during CIR intervals. This excess was interpreted as
544 additional energy input from geomagnetic activity heating. The heating causes a global increase in
545 neutral density, which exceeds 40% at 400 km altitude in the low-latitude dayside ionosphere [Lei *et*
546 *al.*, 2011; Liu *et al.*, 2012b]. The increase of neutral density does not affect the vertical integral of
547 TEC. However, the increase of temperature results in an increase of the recombination rate and, thus,
548 in a decrease of the ionization.

549 On the other hand, a continuous increase of $\Sigma O/N_2$ at low latitudes during RGSs was reported
550 [Crowley *et al.*, 2008; Liu *et al.*, 2012b]. The change of chemical composition of neutral species is
551 attributed to dawnward vertical winds, which carry atomic-oxygen-rich air to lower latitudes that
552 result in enhancements in F-region electron densities. The vertical winds are primarily driven by

553 meridional neutral winds blowing toward equator from the hot auroral regions where Joule and
554 particle heating is produced by continuous geomagnetic activity.

555 Hence in the beginning of recurrent storms, the VTEC dynamics are affected by two opposite factors:
556 atmospheric heating, which increases the recombination rate, and downward vertical winds enriched
557 by atomic oxygen, which increase the electron density. In addition, dayside VTEC enhancements,
558 observed sometimes during CIR intervals, can be produced by strong PPEF of interplanetary origin
559 and/or by the enhancements of solar radiation flux $F_{10.7}$ (see Figures 3 and 4).

560 The CIR interval is followed by HSS. During HSS, VTEC increases substantially in the maximum of
561 RGSs and peaks during the recovery phase of RGSs on the third day after the onset (see Figure 8).

562 From analysis of EC vertical profiles derived from two independent methods of ionosondes and
563 COSMIC/FORMOSAT-3 RO technique, we have found that the maximum of RGS-related positive
564 ionospheric storm is characterized by ~50% increase in VTEC, elevations of hmF2 by a few tens of
565 kilometers and thickening of the F2 layer, while the latitude of crests remains practically
566 unchangeable. This pattern is very close to that revealed by *Ram et al.* [2010] from
567 COSMIC/FORMOSAT-3 RO measurements of the ionospheric disturbances during RGSs. It was
568 suggested that the observed changes in EC could be related to enhancements in the thermospheric
569 temperature and neutral composition $\Sigma O/N_2$. Note that *Ram et al.* [2010] did not distinguish between
570 CIR and HSS intervals.

571 In the low-latitude thermosphere, HSS intervals are accompanied by a decrease of the density and
572 temperature [*Verkhoglyadova et al.*, 2011, *Liu et al.* 2012b]. Hence, higher peak and scale heights of
573 the F2 layer in the maximum of the ionospheric storm cannot be explained by the thermospheric
574 factors. However, an excess of the ratio $\Sigma O/N_2$ at low latitudes still persists [*Crowley et al.*, 2008;
575 *Liu et al.* 2012b]. The excess of $\Sigma O/N_2$ results from continuous heating at middle and high latitudes
576 produced by geomagnetic activity [*Sojka et al.*, 2009; *Verkhoglyadova et al.*, 2011], which is

577 generated by high-amplitude IMF variations inherent to HSS. The high ratio $\Sigma O/N_2$ can explain an
578 increase of VTEC but it is unable to explain the changes of peak and scale heights.

579 The elevation of nmF2 and thickening of the F2 layer as well as increase of VTEC might be also
580 related to intensification of the fountain effect. Note that the effect of DDEF in the noon, postnoon
581 and dusk regions results in suppression or even reversal of the eastward equatorial electrojet and,
582 thus, this mechanism causes a suppression of the fountain effect [Huang *et al.*, 2005; Huang, 2012].

583 The fountain effect on the dayside could be intensified by a prompt penetrating IEF (PPEF) of
584 eastward direction. Studying GIMs with 2-hour resolution does not allow for detecting directly the
585 effect of PPEF. During RGS, the effect is of short duration because of quickly varying IMF B_z . In
586 Figure 8, one can see that the daily maximum values of negative B_z remain strong within three days
587 after the RGS onset. Hence, the observed enhancements of 2-hour averaged VTEC might manifest in
588 the operation of eastward PPEF somewhere within the 2-hour interval.

589 We have found that the maximum of positive ionospheric storm in the crest regions occurs on the
590 day of the maximum solar wind velocity (see Figure 8) on the recovery phase of RGS. The long-
591 lasting recovery phase of RGSs is produced by HILDCAAs, which in turn are related to HSSs
592 characterized by large variations of IEF. Ultra-low-frequency fluctuations of IEF have a substantial
593 effect on global convection and are an important contributor to the large-scale transfer of solar wind
594 energy to the magnetosphere-ionosphere system [Lyons *et al.*, 2009]. Hence, the fountain effect
595 might be intensified by penetrating electric fields of the magnetospheric origin associated with the
596 enhanced convection during HSSs.

597 The close relationship between the positive ionospheric storms and recurrent geomagnetic activity is
598 revealed in seasonal variations. Namely, we have shown that in March 2008 (Figure 3), the
599 enhancements of VTEC were much stronger than those in January 2007 (Figure 4) despite the fact
600 that the level of solar radiation was almost the same ($F_{10.7} \sim 80$). That is a manifestation of a
601 semiannual variation in the ionosphere with maxima in equinoxes. During magnetic quiet times, the

602 ionospheric semiannual variation is originated from variation of circulation pattern controlling the
603 atomic/molecular ratio in the thermosphere [Rishbeth *et al.*, 2000]. During geomagnetic disturbances,
604 it is believed that the semiannual variation in the low-latitude ionosphere is contributed by a
605 semiannual variation of geomagnetic activity caused by a strong coupling of the magnetosphere with
606 the heliospheric driving parameters during equinoxes [Rishbeth and Mendillo, 2001; O'Brien and
607 McPherron, 2002; Emery *et al.*, 2011].

608 We have also found a strong longitudinal variation both in the mean VTEC and in the magnitude of
609 storm-time VTEC enhancements in the crest regions (see Figure 7). In our analysis, the ionospheric
610 storms are characterized by daily maxVTEC, which occurs at roughly the same local times (noon and
611 postnoon sectors) each day. Hence, we are implicitly sampling the ionosphere in a constant local
612 time reference frame. In such a constant local time frame, various nonmigrating tidal components
613 (either propagating upwards from the lower atmosphere or generated in-situ in the ionosphere) will
614 alias into stationary planetary wave components [e.g. Rishbeth and Mendillo, 2001; Forbes *et al.*,
615 2006; Liu *et al.*, 2010b]. During equinoxes, the typical longitudinal variability associated with lower
616 atmospheric tides should be wave-3 and wave-4. The tide-related waves are mainly attributed to
617 magnetic quiet periods with $K_p < 3$ and the amplitude of these waves is relatively small [Kil *et al.*,
618 2012]. Lin *et al.* [2007] reported the maximal amplitude of the wave-4 variation in the postnoon
619 sector to be ~ 3.5 TECU.

620 As shown in Figure 7, the longitudinal variations of the median and of the average enhancements of
621 maxVTEC are about 2 and 3 TECU, respectively. In other words, the average longitudinal variations
622 of maxVTEC during RGSs are comparable with the maximal amplitude of the tide-related wave-4.
623 However, it is difficult to find the wave-3 and wave-4 in Figures 7, 9, 10 and 11, which seem to be
624 mostly wave-1 and wave-2. Namely, in Figure 7 one can distinguish a prominent minimum in the
625 longitudinal range from -60° to 60° and one or two maxima at other longitudes. In Figures 9, 10, 11,
626 we can find either a wave-1 with single maximum and minimum or wave-2 with two maxima and

627 minima. This is not entirely unexpected as past studies have found that the wave-3 and wave-4
628 components in GIM TECs tend to be underestimated compared to those retrieved from satellite
629 observations [Jee *et al.*, 2010; Chang *et al.*, 2013].

630 Figure 6 shows that the storm-time variations of maxVTEC can often exceed 10 TECU. It means that
631 the effect of lower atmospheric tides alone is insufficient to explain the strong longitudinal variation
632 of the VTEC during RGSs and, thus, other mechanisms should be considered. The lack of wave-3
633 and wave-4 might be explained by the geomagnetic nature of the VTEC variations. It is also
634 consistent with the heliospheric and geomagnetic variables that we are correlating. Those variables,
635 responsible for the geomagnetic disturbances, cannot capture the wave-3 and wave-4 perturbations
636 produced by lower atmospheric sources.

637 We have found that during RGSs, the wave-1 and wave-2 are most common and prominent
638 statistically. The positive ionospheric storms have been found to be much stronger in the longitudinal
639 ranges from -150° to -90° and from 90° to 150° than those in the range from -60° to 60° (see Figure
640 7). We have also found two distinct longitudinal ranges, where parameters of different origin play a
641 major role. Namely, in the range of longitudes from -90° to 90° , maxVTEC correlates better with the
642 solar radiation parameter $F10.7$. In the longitudinal range from 90° to -90° , the correlation with the
643 solar radiation decreases dramatically and the influence of heliospheric and geomagnetic parameters
644 becomes important. We have to point out that this pattern of longitudinal variation does not depend
645 much on the season.

646 Similar longitudinal variation with a prominent minimum in the longitudinal range from -60° to 60°
647 was found by Liu *et al.* [2011] for the average low-latitude NmF2 derived from
648 COSMIC/FORMOSAT-3 RO measurements. It is important to point out that those space-borne
649 measurements did not suffer from the non-uniform longitudinal coverage. Liu *et al.* [2011] also
650 demonstrated that hmF2 in the American sector is higher by several tens of kilometers than that in
651 the Pacific region. In Figure 13, we have found the same difference. It was suggested that the wave-

652 like longitudinal feature in the mean NmF2 and hmF2 is most likely associated with the ionosphere-
653 atmosphere couplings with sources of lower atmospheric origins, such as the migrating diurnal tides
654 and planetary waves propagating upward to the ionosphere [*Immel et al.*, 2006; *Liu et al.*, 2011]].
655 However, atmospheric tides cannot explain the maxVTEC variations in relation to the geomagnetic
656 activity, which does not affect the lower atmosphere.

657 *Kil et al.* [2012] ruled out the possibility that the tidal modulation of the dynamo electric fields in the
658 ionosphere is the source of the wave-1 and wave-2 components of longitudinal variations. They
659 suggested mechanisms of the solar zenith angle and magnetic declination, which controls neutral
660 winds and neutral composition at ionospheric heights [*Rishbeth*, 1998]. The effect of solar zenith
661 angle is originated from a difference in the illumination of a dip equator, which governs the EIA
662 region. The dip equator is defined as a line at which the vector of geomagnetic field at given altitude
663 (say 300 km) is strictly horizontal. Because the geomagnetic dipole is tilted and shifted relative to the
664 axis of Earth's rotation, the dip coordinates do not coincide with the geographic ones and, thus, the
665 ionospheric dynamics suffers from the effects of magnetic dip and declination [e.g. *Challinor and*
666 *Eccles*, 1971].

667 In addition, our statistical analysis reveals such annual variations as December to February (Dec-Feb)
668 anomaly and spring asymmetry. The seasonal patterns of the ionospheric variations are explained by
669 chemical and dynamic processes through changes in solar zenith angle, thermospheric composition
670 and global circulations [e.g. *Liu et al.*, 2011]. For the spring asymmetry, we have found a lower
671 correlation of maxVTEC with F10.7 and higher anti-correlation with the annual angle. This
672 asymmetry is most prominent in the longitudinal range from 120° to -90°. It seems that in this range,
673 the solar zenith angle plays a more important role during the equinoxes than during solstices.
674 Because of that the lower correlation with the solar radiation index F10.7 is “compensated” by
675 higher anti-correlation with the annual angle.

676 The Dec-Feb anomaly is characterized by higher correlations of maxVTEC with the annual angle
677 and heliospheric and geomagnetic parameters in December - February. Higher correlations with the
678 annual angle, revealed in the longitude range from -90° to 90° , can be explained in the frame of solar
679 zenith angle effect [e.g. Kil et al., 2012]. For the heliospheric and geomagnetic parameters, the Dec-
680 Feb anomaly consists in highest correlations with maxVTEC in the range of longitudes from $\sim 120^\circ$
681 to -90° .

682 Morphologically, the Dec-Feb anomaly is close to an effect of so-called annual asymmetry revealed
683 for quiet geomagnetic conditions [e.g. Mendillo et al., 2005]. Namely, average noon TEC in
684 December substantially exceeds that in June, almost everywhere around the Globe. At low latitudes,
685 the most prominent asymmetry was reported in the longitudinal range from 120° to -60° , i.e.
686 practically in the same range as that for the Dec-Feb effect in maxVTEC. Mendillo et al. [2005]
687 concluded that global changes in the neutral atmosphere (atomic/molecular ratio O/N_2) contribute to
688 the ionospheric annual asymmetry. On the other hand, discussing the driven factors of longitudinal
689 variations of the annual asymmetry, Zeng et al. [2008] pointed out the effects of solar zenith angle,
690 magnetic field configuration and zonal neutral winds.

691 During RGSs, the value of $\Sigma O/N_2$ increases at low latitudes for several days [Crowley et al., 2008;
692 Liu et al., 2012b] that should strengthen the Dec-Feb effect. Hence, higher correlation of maxVTEC
693 with the geomagnetic activity around winter solstice can be related to the storm-time enhancement of
694 $\Sigma O/N_2$ at low latitudes. It might be also possible that meridional equatorward neutral winds enforce
695 zonal neutral winds such that the effect of magnetic declination results in additional contribution to
696 the low-latitude electron density enhancements.

697 It is important to point out that numerous statistical studies of longitudinal variations in the
698 ionosphere did not eliminate the recurrent geomagnetic activity or used a criterion of $K_p < 3$. As one
699 can see in Figure 8, the maximum of positive ionospheric storms corresponds to the average $K_p \sim 3$.
700 Hence, it is important to estimate the contribution of RGSs to the statistics of ionospheric

701 disturbances. For this purpose, we calculate an integral probability of occurrence of solar wind
702 streams with various velocities from 250 to 800 km/s for the time interval from 2004 to 2008 (see
703 Figure 14). Note that the average solar wind speed is ~ 400 km/s [Veselovsky *et al.*, 2010].
704 HILDCAAs are related to solar streams with speed >400 km/s [Tsurutani *et al.*, 1995]. In Figures 3
705 and 4, one can clearly see that positive ionospheric storms persist during whole intervals of
706 HILDCAAs and even 1 to 2 days longer. Hence, we can estimate approximately that the occurrence
707 of positive ionospheric storms corresponds to the occurrence of >400 km/s solar wind streams. In
708 Figure 14, we find that the probability of such occurrence is 0.6. Note that the integral occurrence
709 probability decreases gradually such that the occurrence of solar wind streams with higher speeds of
710 >500 km/s is still a significant portion ($\sim 30\%$) of the whole statistics.

711 In Figure 14, we also show a scatter plot of 3-hour K_p index versus solar wind speed V_{sw} . On
712 average, K_p increases with V_{sw} . However, the spread is very wide. There are numerous events with
713 small K_p accompanied by high solar wind speed. We have estimated that 33% (39%) of statistics is
714 characterized by $K_p < 3$ ($K_p \leq 3$) under $V_{sw} > 400$ km/s. Such conditions are proper for RGSs and
715 related ionospheric disturbances. As a result, more than $>30\%$ of “quiet” ionospheric conditions
716 determined from $K_p < 3$ can be actually contributed by ionospheric disturbances originated from
717 HSSs.

718 From the above, we realize that the recurrent ionospheric storms at low latitudes result from a
719 complex of competitive phenomena such as thermospheric heating, change of neutral composition
720 $\Sigma O/N_2$, PPEF, penetrating electric fields of the magnetospheric origin related to HILDCAAs, effect
721 of solar zenith angle and probably magnetic declination effect. On the declining phase of solar
722 activity, CIR/HSS result in ionospheric disturbances lasting up to 60% of time or even more. Hence,
723 the recurrent ionospheric storms dominate in the statistics of ionospheric conditions. In this sense,
724 both the equinox maxima in the ionospheric ionization and the Dec-Feb effect of enhanced

725 correlation of TEC with the geomagnetic activity are strongly related to ionospheric disturbances
726 during RGSs.

727

728 **5. Conclusions**

729

730 Analysis of case events and statistics of positive ionospheric storms in the region of dayside
731 equatorial ionization anomaly during recurrent geomagnetic storms on the declining phase of the
732 23rd solar cycle (years from 2004 to 2008) reveals the following:

733 1. During the storm onset related to a co-rotating interaction region, the total electron content
734 increases slightly or even decreases. The suppression might be caused by a strong heating of the low-
735 latitude thermosphere.

736 2. Positive ionospheric storms appear as substantial enhancements of the total electron content within
737 a few days (1 – 4 days) after the storm onset during high-intensity long-duration continuous auroral
738 activity produced by high-speed solar wind streams. On average, the maximum of positive
739 ionospheric storms occurs 3 days after the onset and on the recovery phase of recurrent magnetic
740 storms, at the day of maximum solar wind velocity.

741 3. In the maximum of ionospheric storm occurred during Whole Heliospheric Interval and related to
742 HSS, we find that at substantially different longitudes, the F2 layer is thickening, NmF2 increases by
743 ~50% and hmF2 elevates by a few tens of kilometers. We speculate that this might result from the
744 increase of $\Sigma O/N_2$ and penetrating electric fields of interplanetary and magnetospheric origin.

745 4. Statistically, the response of positive ionospheric storms to solar, heliospheric and geomagnetic
746 drivers has a prominent longitudinal asymmetry. In the longitudinal range from -90° to 90° , the solar
747 illumination plays a major role. In the range of longitudes from 90° to 180° and from -180° to -120° ,
748 the influence of heliospheric and geomagnetic drivers becomes significant.

749 5. Months from December to February are characterized by the highest correlations of the
750 ionospheric ionization enhancements with the heliospheric and geomagnetic drivers.

751
752
753 **Acknowledgements** The authors thank Kyoto World Data Center for Geomagnetism
754 (<http://swdcwww.kugi.kyoto-u.ac.jp/index.html>) for providing the *Dst*, *Kp* and *AE* geomagnetic
755 indices. The Global Ionosphere Maps/VTEC Data are produced by European Data Center
756 (<http://www.aiub.unibe.ch/ionosphere/>). The ACE solar wind data were provided by N. Ness and D.J.
757 McComas through the CDAWeb website. We thank Dr. N. Balan for very useful discussion and
758 valuable recommendations. This work was supported by grants NSC-100-2119-M-008 -019- from
759 the National Science Council of Taiwan and by Ministry of Education under the Aim for Top
760 University program at National Central University of Taiwan.

761

762 **References**

- 763
764 A, E., et al. (2012), A global model: Empirical orthogonal function analysis of total electron content
765 1999-2009 data, *J. Geophys. Res.*, 117, A03328, doi:10.1029/2011JA017238.
- 766 Blanc, M. and A.D. Richmond (1980), The ionospheric disturbance dynamo, *J. Geophys. Res.*,
767 85(A4), 1669-1686, doi:10.1029/JA085iA04p01669.
- 768 Borovsky, J. E., and M. H. Denton (2006), Differences between CME-driven storms and CIR-driven
769 storms, *J. Geophys. Res.*, 111, A07S08, doi:10.1029/2005JA011447.
- 770 Bothmer V., et al. (2004), The solar and interplanetary causes of space storms in solar cycle 23,
771 *IEEE Transactions on Plasma Science*, 32(4), Part 1, 1411 - 1414.
- 772 Burke, W. J., L. C. Gentile, and M. P. Hagan (2010), Thermospheric heating by high-speed streams
773 in the solar wind, *J. Geophys. Res.*, 115, A06318, doi:10.1029/2009JA014585.

774 Burlaga, L.F., and R. P. Lepping (1977), The causes of recurrent geomagnetic storms, *Planet. Space*
775 *Sci.*, 25, 1151.

776 Burns, A. G., et al. (2012), The effects of corotating interaction region/high speed stream storms on
777 the thermosphere and ionosphere during the last solar minimum, *J. Atmos. Solar-Terr. Phys.*, 83,
778 79-87, doi:10.1016/j.jastp.2012.02.006.

779 Challinor, R. A. and D. Eccles (1971), Longitudinal variations of the mid-latitude ionosphere
780 produced by neutral-air winds-I. Neutral-air winds and ionospheric drifts in the northern and
781 southern hemispheres, *J. Atmos. Solar-Terr. Phys.*, 33(3), 363-369.

782 Chang, L. C., et al. (2009), Isolation of the global MLT thermal response to recurrent geomagnetic
783 activity, *Geophys. Res. Lett.*, 36, L15813, doi:10.1029/2009GL039305.

784 Chang, L.C., C.H. Lin, and J.Y. Liu (2013), A Statistical Comparison of Zonal Mean and Tidal
785 Signatures in FORMOSAT-3/COSMIC and Ground-Based GPS TECs, *Terr. Atmos. Ocean Sci.*,
786 24 (2), 253-263, doi:10.3319/TAO.2012.10.17.01(SEC).

787 Crowley, G., et al. (2008), Periodic modulations in thermospheric composition by solar wind high
788 speed streams, *Geophys. Res. Lett.*, 35, L21106, doi:10.1029/2008GL035745.

789 Deng, Y., et al. (2011), Energy input into the upper atmosphere associated with high-speed solar
790 wind streams in 2005, *J. Geophys. Res.*, 116, A05303, doi:10.1029/2010JA016201.

791 Denton, M. H., T. Ulich, and E. Turunen (2009), Modification of midlatitude ionospheric parameters
792 in the F2 layer by persistent high-speed solar wind streams, *Space Weather*, 7, S04006,
793 doi:10.1029/2008SW000443.

794 Emery, B. A., et al. (2011), Solar rotational periodicities and the semiannual variation in the solar
795 wind, radiation belt, and aurora, *Solar Phys.*, 274, 399-425, doi:10.1007/s11207-011-9758-x.

796 Forbes, J. M., E. P. Scott, and Z. Xiaoli (2000), Variability of the ionosphere, *J. Atmos. Solar-Terr.*
797 *Phys.*, 62, 685-693.

798 Forbes, J. M., et al. (2006), Troposphere-thermosphere tidal coupling as measured by the SABER
799 instrument on TIMED during July-September 2002, *J. Geophys. Res.*, 111, A10S06,
800 doi:10.1029/2005JA011492.

801 Fuller-Rowell, T., et al. (1994), Response of the Thermosphere and Ionosphere to Geomagnetic
802 Storms, *J. Geophys. Res.*, 99(A3), 3893-3914.

803 Galkin, I. A., et al. (2008), The ARTIST 5, in *Radio Sounding and Plasma Physics*, AIP Conf. Proc.
804 974, 150-159

805 Guo J., et al. (2011), Interplanetary drivers of ionospheric prompt penetration electric fields, *J. Atmos.*
806 *Solar-Terr. Phys.*, 73, 130–136.

807 Hajj, G. A., et al. (2000), COSMIC GPS ionospheric sensing and space weather, *Terrestrial,*
808 *Atmospheric and Oceanic Sciences*, 11(1), 235-272.

809 Hernandez-Pajares, M., et al. (2009), The IGS VTEC maps: A reliable source of ionospheric
810 information since 1998, *J. Geod.*, 83, 263–275, doi:10.1007/s00190-008-0266-1.

811 Huang, C.-M., A. D. Richmond, and M.-Q. Chen (2005), Theoretical effects of geomagnetic activity
812 on low-latitude ionospheric electric fields, *J. Geophys. Res.*, 110, A05312,
813 doi:10.1029/2004JA010994.

814 Huang, C.-S. (2012), Equatorial ionospheric electrodynamics associated with high-speed solar wind
815 streams during January-April 2007, *J. Geophys. Res.*, 117, A10311, doi:10.1029/2012JA017930.

816 Immel, T. J., et al. (2006), Control of equatorial ionospheric morphology by atmospheric tides,
817 *Geophys. Res. Lett.*, 33, L15108, doi:10.1029/2006GL026161.

818 Jee, G., et al. (2010), Assessment of GPS global ionosphere maps (GIM) by comparison between
819 CODE GIM and TOPEX/Jason TEC data: Ionospheric perspective, *J. Geophys. Res.*, 115,
820 A10319, doi:10.1029/2010JA015432.

821 Kil, H., et al. (2012), Persistent longitudinal features in the low-latitude ionosphere, *J. Geophys. Res.*,
822 117, A06315, doi:10.1029/2012JA017570.

823 Koga D., et al. (2011), Electrodynamic coupling processes between the magnetosphere and the
824 equatorial ionosphere during a 5-day HILDCAA event, *J. Atmos. Solar-Terr. Phys.*, 73, 148–155.

825 Kuznetsov, S. N., A. V. Suvorova, E. D. Tolstaya (1993), Relationship of the cleft latitude to
826 interplanetary parameters and *Dst*-variations, *Cosm. Res.*(English thransl), 31, 4, 409-415.

827 Lei, J., et al. (2008a), Rotating solar coronal holes and periodic modulation of the upper atmosphere,
828 *Geophys. Res. Lett.*, 35, L10109, doi:10.1029/2008GL033875.

829 Lei, J., et al. (2008b), Ionosphere response to solar wind high-speed streams, *Geophys. Res. Lett.*, 35,
830 L19105, doi:10.1029/2008GL035208.

831 Lei, J., et al. (2008c), Global thermospheric density variations caused by high-speed solar wind
832 streams during the declining phase of solar cycle 23, *J. Geophys. Res.*, 113, A11303,
833 doi:10.1029/2008JA013433.

834 Lei, J., et al. (2011), Impact of CIR storms on thermosphere density variability during the solar
835 minimum of 2008, *Sol. Phys.*, 274, 427-437, doi:10.1007/s11207-010-9563-y.

836 Lin, C. H., et al. (2007), Longitudinal structure of the equatorial ionosphere: Time evolution of the
837 four-peaked EIA structure, *J. Geophys. Res.*, 112, A12305, doi:10.1029/2007JA012455.

838 Liu, L., and Y. Chen (2009), Statistical analysis of solar activity variations of total electron content
839 derived at Jet Propulsion Laboratory from GPS observations, *J. Geophys. Res.*, 114, A10311,
840 doi:10.1029/2009JA014533.

841 Liu, J., et al. (2010a), Response of the topside ionosphere to recurrent geomagnetic activity, *J.*
842 *Geophys. Res.*, 115, A12327, doi:10.1029/2010JA015810.

843 Liu, H., S. V. Thampi, and M. Yamamoto (2010b), Phase reversal of the diurnal cycle in the
844 midlatitude ionosphere, *J. Geophys. Res.*, 115, A01305, doi:10.1029/2009JA014689.

845 Liu, L., et al. (2011), Features of the middle- and low-latitude ionosphere during solar minimum as
846 revealed from COSMIC radio occultation measurements, *J. Geophys. Res.*, 116, A09307,
847 doi:10.1029/2011JA016691.

848 Liu, J., et al. (2012a), High-speed stream impacts on the equatorial ionization anomaly region during
849 the deep solar minimum year 2008, *J. Geophys. Res.*, 117, A10304,
850 doi:10.1029/2012JA018015.

851 Liu, J., et al. (2012b), Superposed epoch analyses of thermospheric response to CIRs: Solar cycle
852 and seasonal dependencies, *J. Geophys. Res.*, 117, A00L10, doi:10.1029/2011JA017315

853 Lyons, L. R., et al. (2009), Evidence that solar wind fluctuations substantially affect global
854 convection and substorm occurrence, *J. Geophys. Res.*, 114, A11306,
855 doi:10.1029/2009JA014281.

856 Mendillo, M., et al. (2005), The global ionospheric asymmetry in total electron content, *J. Atmos.*
857 *Solar-Terr. Phys.*, 67, 1377-1387.

858 Mlynczak, M. G., et al. (2008), Solar-terrestrial coupling evidenced by periodic behavior in
859 geomagnetic indexes and the infrared energy budget of the thermosphere, *Geophys. Res. Lett.*,
860 35, L05808, doi:10.1029/2007GL032620.

861 Newell, P. T., et al. (2008), Pairs of solar wind-magnetosphere coupling functions: Combining a
862 merging term with a viscous term works best, *J. Geophys. Res.*, 113, A04218,
863 doi:10.1029/2007JA012825.

864 O'Brien, T. P., and R. L. McPherron (2002), Seasonal and diurnal variation of Dst dynamics, *J.*
865 *Geophys. Res.*, 107(A11), 1341, doi:10.1029/2002JA009435.

866 Ozguc, A., T. Atac, and R. Pektas (2008), Examination of the solar cycle variation of foF2 for cycles
867 22 and 23, *J. Atmos. Solar-Terr. Phys.*, 70, 268-27.

868 Pedatella, N. M., and J. M. Forbes (2011), Electrodynamic response of the ionosphere to high-speed
869 solar wind streams, *J. Geophys. Res.*, 116, A12310, doi:10.1029/2011JA017050.

870 Pedatella, N. M., et al. (2010), Ionosphere response to recurrent geomagnetic activity: Local time
871 dependency, *J. Geophys. Res.*, 115, A02301, doi:10.1029/2009JA014712.

872 Ram, T., et al. (2010), Dayside ionospheric response to recurrent geomagnetic activity during the
873 extreme solar minimum of 2008, *Geophys. Res. Lett.*, 37, L02101, doi:10.1029/2009GL041038.

874 Rebischung, P., et al. (2012), IGS08: the IGS realization of ITRF2008, *GPS Solut.*, 16, 483-494, DOI
875 10.1007/s10291-011-0248-2.

876 Richardson, I. G., et al. (2006), Major geomagnetic storms (Dst <-100 nT) generated by corotating
877 interaction regions, *J. Geophys. Res.*, 111, A07S09, doi:10.1029/2005JA011476.

878 Rishbeth, H., (1998), How the thermospheric circulation affects the ionospheric F2-layer, *J. Atmos.*
879 *Solar-Terr. Phys.*, 60, 1385 - 1402.

880 Rishbeth, H., and M. Mendillo (2001), Patterns of F2-layer variability, *J. Atmos. Solar-Terr. Phys.*, 63,
881 1661-1680.

882 Rishbeth, H., et al. (2000), Annual and semiannual variations in the ionospheric F2-layer: II. Physical
883 discussion, *Ann. Geophys.*, 18, 945-956.

884 Sojka, J. J., et al. (2009), Observations of ionospheric heating during the passage of solar coronal hole
885 fast streams, *Geophys. Res. Lett.*, 36, L19105, doi:10.1029/2009GL039064.

886 Thayer, J. P., et al. (2008), Thermospheric density oscillations due to periodic solar wind high-speed
887 streams, *J. Geophys. Res.*, 113, A06307, doi:10.1029/2008JA013190.

888 Tsai, L.-C., et al. (2006), Ionospheric tomography of the reference GPS/MET experiment through the
889 IRI model, *Terrestrial, Atmospheric and Oceanic Sciences*, 17(1), 263-276.

890 Tsurutani, B. T., et al. (1995), Interplanetary Origin of Geomagnetic Activity in the Declining Phase
891 of the Solar Cycle, *J. Geophys. Res.*, 100(A11), 21717-21733.

892 Tsurutani, B. T., et al. (2011a), The properties of two solar wind high speed streams and related
893 geomagnetic activity during the declining phase of solar cycle 23, *J. Atmos. Solar-Terr. Phys.*, 73
894 164–177.

895 Tsurutani, B. T., Echer, E., and Gonzalez, W. D. (2011b), The solar and interplanetary causes of the
896 recent minimum in geomagnetic activity (MGA23): a combination of midlatitude small coronal

897 holes, low IMF BZ variances, low solar wind speeds and low solar magnetic fields, *Ann.*
898 *Geophys.*, 29, 839-849, doi:10.5194/angeo-29-839-2011

899 Turner, N. E., et al. (2009), Geoefficiency and energy partitioning in CIR-driven and CME-driven
900 storms, *J. Atmos. Solar-Terr. Phys.*, 71, 1023-1031.

901 Verkhoglyadova, O. P., et al. (2011), Ionospheric VTEC and thermospheric infrared emission
902 dynamics during corotating interaction region and high-speed stream intervals at solar minimum:
903 25 March to 26 April 2008, *J. Geophys. Res.*, 116, A09325, doi:10.1029/2011JA016604.

904 Verkhoglyadova, O. P., et al. (2013), Variability of ionospheric TEC during solar and geomagnetic
905 minima (2008 and 2009): external high speed stream drivers, *Ann. Geophys.*, 31, 263-276,
906 doi:10.5194/angeo-31-263-2013.

907 Veselovsky, I. S., A. V. Dmitriev, and A. V. Suvorova (2010), Algebra and Statistics of the Solar
908 Wind, *Cos. Res.*, 48(2), 113-128, DOI: 10.1134/S0010952510020012.

909 Wang, W., et al. (2011), Ionospheric day-to-day variability around the whole heliosphere interval in
910 2008, *Sol. Phys.*, 274, 457-472, doi:10.1007/s11207-011-9747-0.

911 Zeng, Z., et al. (2008), Ionospheric annual asymmetry observed by the COSMIC radio occultation
912 measurements and simulated by the TIEGCM, *J. Geophys. Res.*, 113, A07305,
913 doi:10.1029/2007JA012897.

914

915 Table 1. Number of low- to mid-latitude IGS receivers in different longitudinal ranges

-180°	-150°	-120°	-90°	-60°	-30°	0°	30°	60°	90°	120°	150°
-150°	-120°	-90°	-60°	-30°	0°	30°	60°	90°	120°	150°	180°
6	4	8	10	6	6	10	11	9	10	11	5

916

917 **Figure Captions**

918
919 Figure 1. Solar-cycle variations of solar radio flux F10.7 (top panel), solar wind speed (middle panel)
920 and daily minimum Dst index (bottom panel). The interval used for analysis from 2004 to 2008
921 (indicated by red) corresponds to declining phase and solar minimum accompanied by co-rotating
922 high-speed solar wind streams and recurrent geomagnetic storms (RGSs) of moderate and low
923 intensity ($Dst_{min} > -70$ nT as indicated by the dashed line at the bottom panel).

924
925 Figure 2. Global ionospheric maps (GIMs) of vertical total electron content (VTEC) constructed at
926 22 UT (left) and 8 UT (right) during (a) quiet day on 25 March 2008, (b) disturbed days on 27 (left)
927 and 29 (right) March 2008, and (c) residual between the disturbed and quiet days. March 27 and 29
928 correspond, respectively, to maximum and recovery phase of the storm (see Figure 3). The dip
929 equator is shown by the white curve. Vertical black dashed lines indicate local noon. Strong positive
930 ionospheric storms occur at low latitudes in the postnoon and evening sectors in Indochina, Pacific,
931 and American regions (at longitudes from 60° to -60°).

932
933 Figure 3. 27-day interval of solar, heliospheric, geomagnetic and ionospheric variations from 20
934 March to 15 April 2008 (from top to bottom): solar radio flux F10.7, solar wind velocity, density,
935 IMF Bz component in GSM, geomagnetic indices AE, Dst, daily maximum VTEC (solid curve) and
936 variations of VTEC (colored 2D histogram) in longitudinal ranges from -120° to -90° , from 90° to
937 120° and from -30° to 0° . The black stars indicate maxima of VTEC (maxVTEC). The red stars
938 indicate the corresponding magnitude of external parameters (see details in the text). The red vertical
939 arrows indicate the onset of RGSs. The blue circles depict suppressions of maxVTEC in the
940 beginning of RGSs. Peak values of maxVTEC are indicated by the red circles. maxVTEC increases

941 both during enhancements of the solar radiation (F10.7) and during RGSs. In different latitudinal
942 ranges, maxVTEC increases in different manner both temporally and spatially.

943
944 Figure 4. The same as in Figure 3 but for the interval from 1 January to 3 February 2007 and
945 longitudinal ranges for maxVTEC from -150° to -120° , from 120° to 150° and from 0° to 30° .
946 Variations of maxVTEC exhibit similar spatial and temporal patterns.

947
948 Figure 5. Universal time distribution for the onsets of 185 recurrent geomagnetic storms occurred
949 from 2004 to 2008. The RGS onsets are practically equally probable at different UT.

950
951 Figure 6. Superposed epoch analysis of *Dst* (top panel) and maxVTEC variations at longitudes from
952 0° to 30° (middle panel) and from 120° to 150° (bottom panel) during 185 RGSs occurred from 2004
953 to 2008. Variations during different storms are shown by thin curves. The daily medians are
954 indicated by thick red curves. On the top panel, the white dashed and red solid curves depict the
955 median of hourly averaged and of daily minimum *Dst*, respectively. The onset of RMS corresponds
956 to day = 0. The amplitude of median maxVTEC variations in the longitudinal range from 120° to
957 150° is about 30% higher than that in the range from 0° to 30° .

958
959 Figure 7. Longitudinal variations of average maxVTEC characteristics during RGSs occurred from
960 2004 to 2008. Upper panel shows the amplitudes of median maxVTEC variations (solid histogram,
961 left axis) and variation of median maxVTEC during RGS onsets (day = 0) (dashed histogram, right
962 axis). Lower panel shows the mean maxVTEC (solid histogram, left axis) and average enhancements
963 of maxVTEC (dashed histogram, right axis). Bold numbers indicate the amount of receivers in each
964 longitudinal range. The longitudinal range from -60° to 60° is characterized by lowest variability of
965 maxVTEC.

966
967 Figure 8. Average variations of various parameters during 185 RGSs occurred from 2004 to 2008
968 (from top to bottom): maximal solar wind velocity (solid curve, left axis) and density (dashed curve,
969 right axis); minimal Dst (solid curve, left axis) and maximal Kp (dashed curve, right axis); maximal
970 AE (solid curve, left axis) and minimal Bz (dashed curve, right axis); median maxVTEC in various
971 longitudinal ranges (solid and dashed curves correspond to eastern and western longitudes,
972 respectively). The onset of RMS corresponds to the day = 0 (vertical dashed line). Geomagnetic
973 indices peak one day after the onset. Maximum of the solar wind velocity and maxVTEC occur 2
974 days after the onset (indicated by vertical solid line).

975
976 Figure 9. Correlation of maxVTEC with various parameters: (a) all set of parameters and a function
977 of F10.7, (b) AE index and solar wind velocity, (c) Dst index and cosine of annual angle (cos).

978
979 Figure 10. Seasonal variation of the correlation between the maxVTEC and (a) all set of parameters
980 and (b) a function of F10.7. maxVTEC has a weaker correlation with F10.7 during spring equinox at
981 all longitudes.

982
983 Figure 11. Seasonal variation of the correlation between the maxVTEC and (a) cosine of annual
984 angle, (b) Dst index, (c) solar wind velocity, and (d) AE index and. The cosine of annual angle shows
985 a strong anti-correlation around spring equinox. High correlations with the solar wind and
986 geomagnetic parameters are found during winter (Dec – Feb), especially in the Pacific and South
987 America regions.

988
989 Figure 12. Height profile of electron content (EC) measured in the Pacific region (a) over Kwajalein
990 (9°N, 167°E) and (b) reconstructed from COSMIC/FORMOSAT-3 radio-occultation tomography at

991 longitude 167°E during a quiet day on 25 March 2008 (right panels) and in the maximum of RGS-
992 related positive ionospheric storm on 28 March 2008 (left panels). During the storm, the EC in the
993 Pacific region increases substantially and the maximum of F-layer elevates up to ~ 50 km from the
994 height of ~250 km to ~300 km.

995
996 Figure 13. The same as in Figure 12, but over Jicamarca (12°S, 77°W) and at longitude 80°W.
997 During the storm, the EC in the South America region increases substantially and the maximum of F-
998 layer elevates up to ~ 50 km from the height of ~300 km to ~350 km.

999
1000 Figure 14. Integral probabilities: (solid curves, left axis) of occurrence of solar wind streams with
1001 velocities higher than given and (green isolines with numbers, right axis) of K_p smaller than given at
1002 various velocities in 2004 – 2008. Dots depict the scatter plot of K_p versus speed. High-speed solar
1003 wind streams with velocity >400 km/s (depicted by red curve) occur in 60% of statistics. More than
1004 30% of statistics is characterized by small $K_p < 3$ under high-speed solar wind streams that is proper
1005 for RGSs.

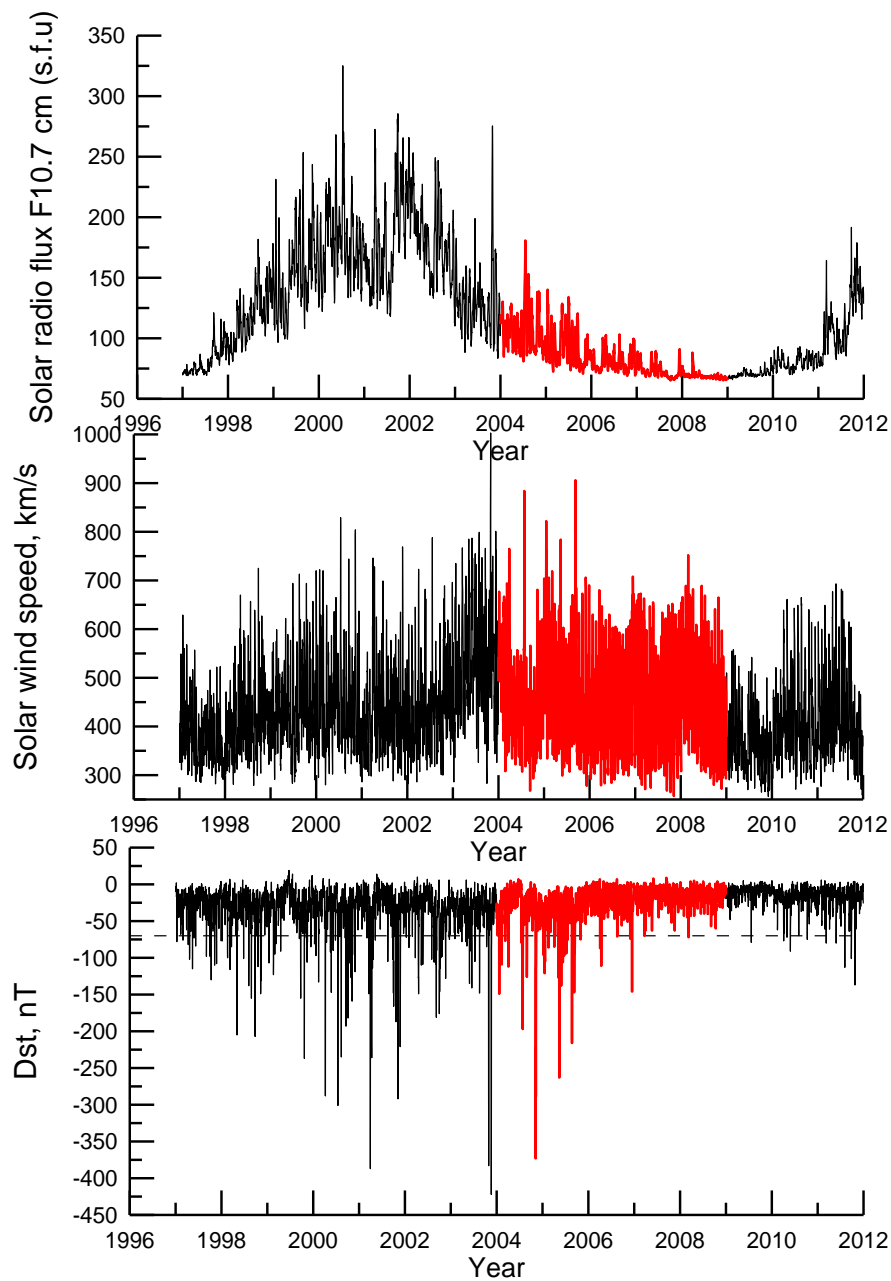


Figure 1. Solar-cycle variations of solar radio flux F10.7 (top panel), solar wind speed (middle panel) and daily minimum Dst index (bottom panel). The interval used for analysis from 2004 to 2008 (indicated by red) corresponds to declining phase and solar minimum accompanied by co-rotating high-speed solar wind streams and recurrent geomagnetic storms (RGSs) of moderate and low intensity ($Dst_{min} > -70$ nT as indicated by the dashed line at the bottom panel).

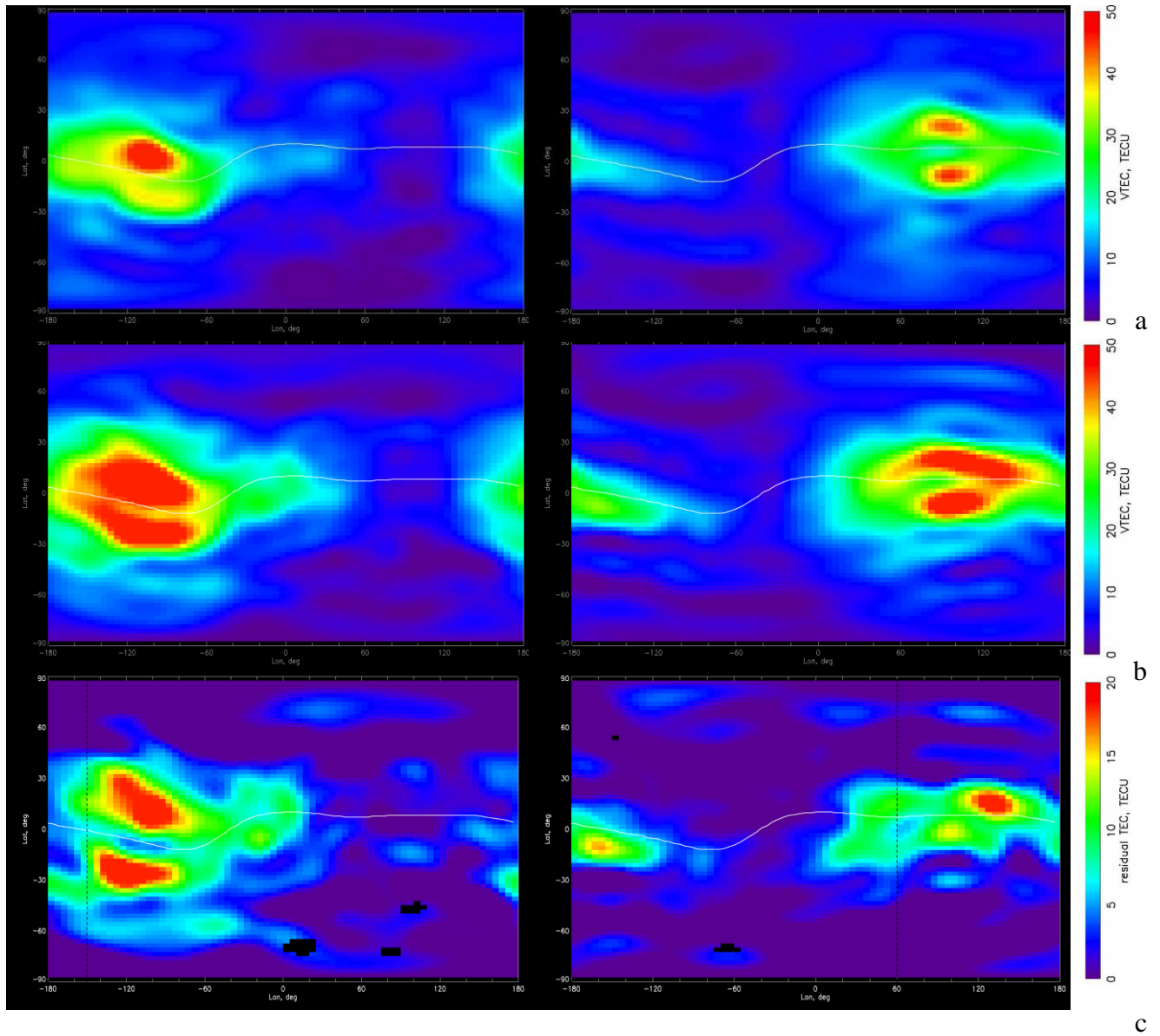


Figure 2. Global ionospheric maps (GIMs) of vertical total electron content (VTEC) constructed at 22 UT (left) and 8 UT (right) during (a) quiet day on 25 March 2008, (b) disturbed days on 27 (left) and 29 (right) March 2008, and (c) residual between the disturbed and quiet days. March 27 and 29 correspond, respectively, to maximum and recovery phase of the storm (see Figure 3). The dip equator is shown by the white curve. Vertical black dashed lines indicate local noon. Strong positive ionospheric storms occur at low latitudes in the postnoon and evening sectors in Indochina, Pacific, and American regions (at longitudes from 60° to -60°).

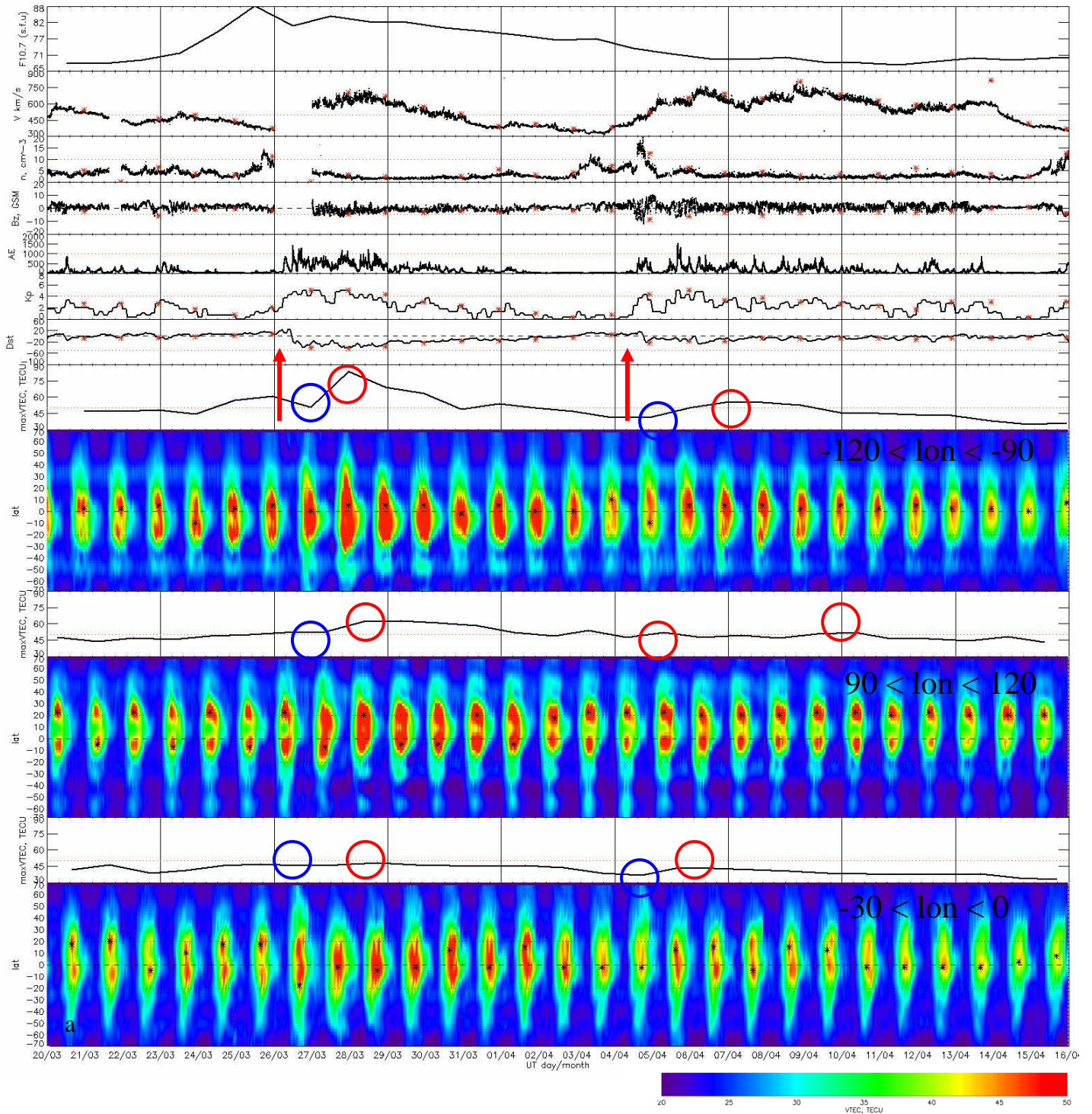


Figure 3. 27-day interval of solar, heliospheric, geomagnetic and ionospheric variations from 20 March to 15 April 2008 (from top to bottom): solar radio flux F10.7, solar wind velocity, density, IMF Bz component in GSM, geomagnetic indices AE, Dst, daily maximum VTEC (solid curve) and variations of VTEC (colored 2D histogram) in longitudinal ranges from -120° to -90° , from 90° to 120° and from -30° to 0° . The black stars indicate maxima of VTEC (maxVTEC). The red stars indicate the corresponding magnitude of external parameters (see details in the text). The red vertical arrows indicate the onset of RGSs. The blue circles depict suppressions of maxVTEC in the beginning of RGSs. Peak values of maxVTEC are indicated by the red circles. maxVTEC increases both during enhancements of the solar radiation (F10.7) and during RGSs. In different latitudinal ranges, maxVTEC increases in different manner both temporally and spatially.

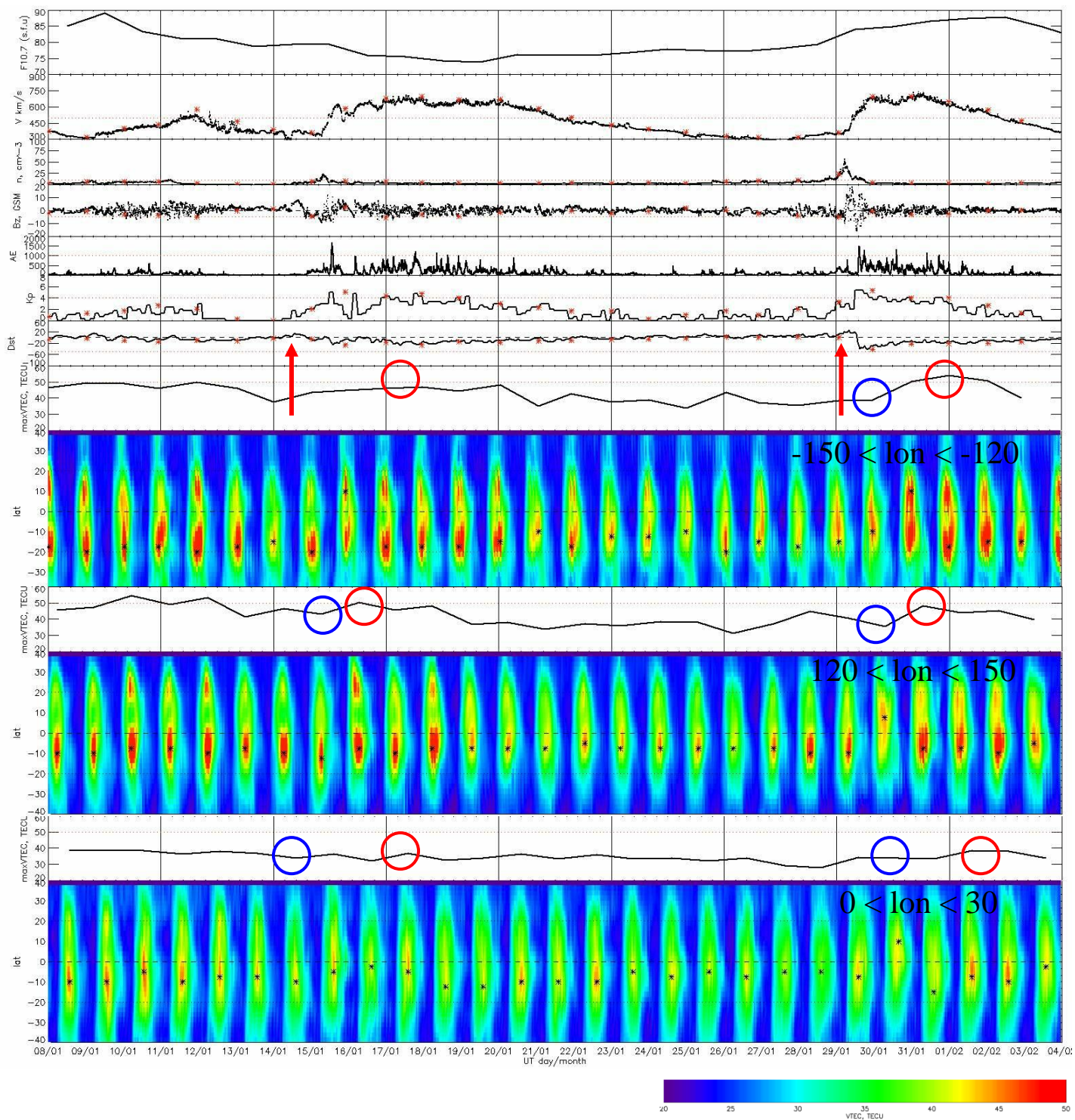


Figure 4. The same as in Figure 3 but for the interval from 1 January to 3 February 2007 and longitudinal ranges for maxVTEC from -150° to -120° , form 120° to 150° and from 0° to 30° . Variations of maxVTEC exhibit similar spatial and temporal patterns.

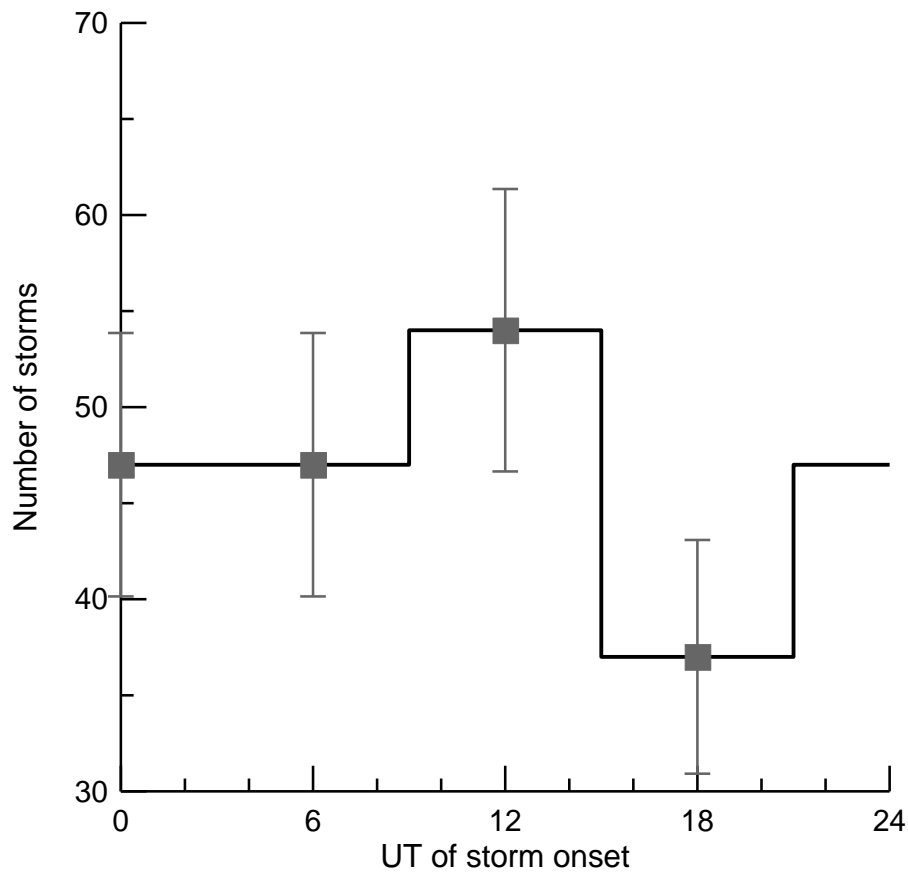


Figure 5. Universal time distribution for the onsets of 185 recurrent geomagnetic storms occurred from 2004 to 2008. The RGS onsets are practically equally probable at different UT.

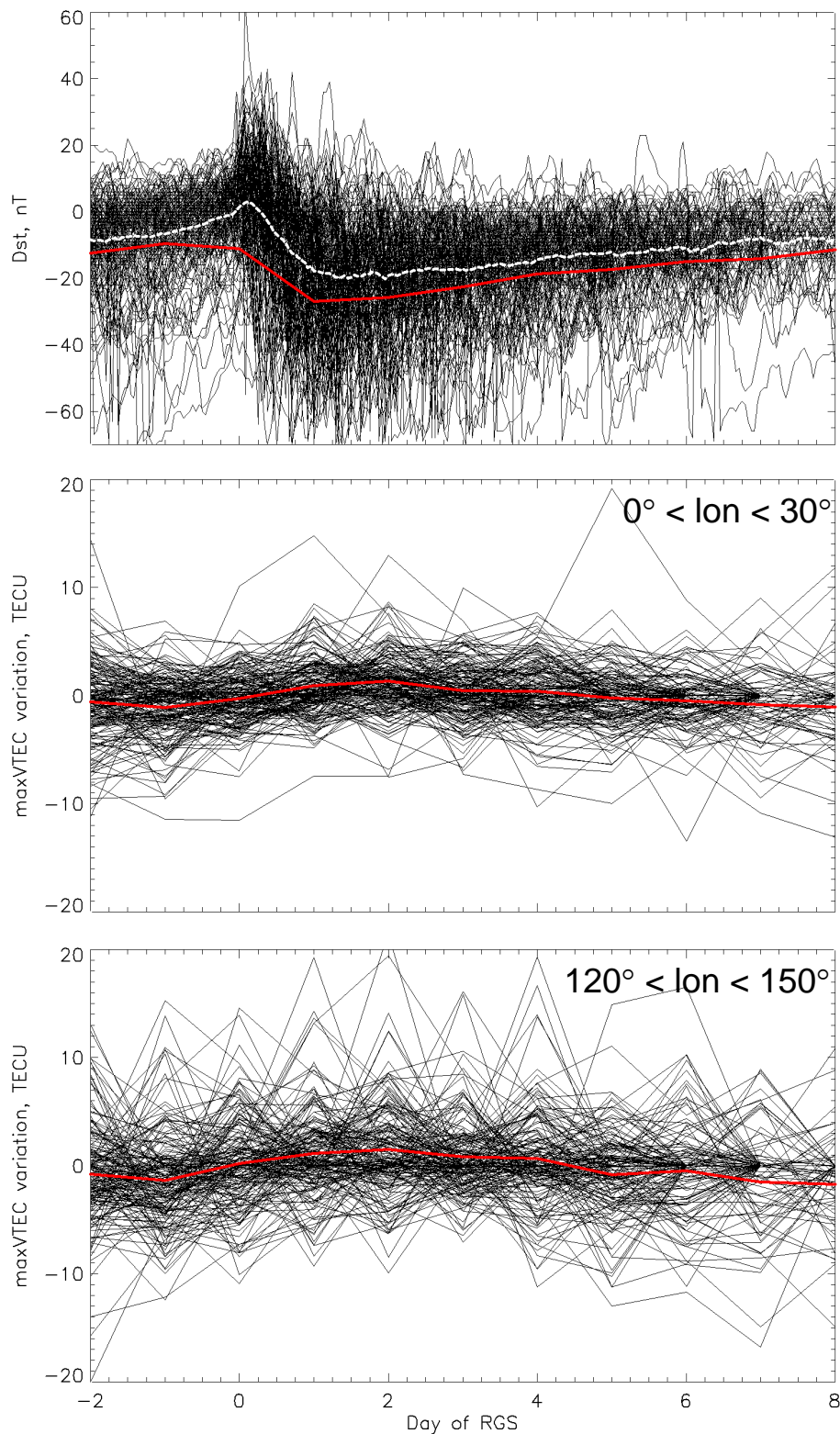


Figure 6. Superposed epoch analysis of Dst (top panel) and maxVTEC variations at longitudes from 0° to 30° (middle panel) and from 120° to 150° (bottom panel) during 185 RGSs occurred from 2004 to 2008. Variations during different storms are shown by thin curves. The daily medians are indicated by thick red curves. On the top panel, the white dashed and red solid curves depict the median of hourly averaged and of daily minimum Dst , respectively. The onset of RMS corresponds to day = 0. The amplitude of median maxVTEC variations in the longitudinal range from 120° to 150° is about 30% higher than that in the range from 0° to 30° .

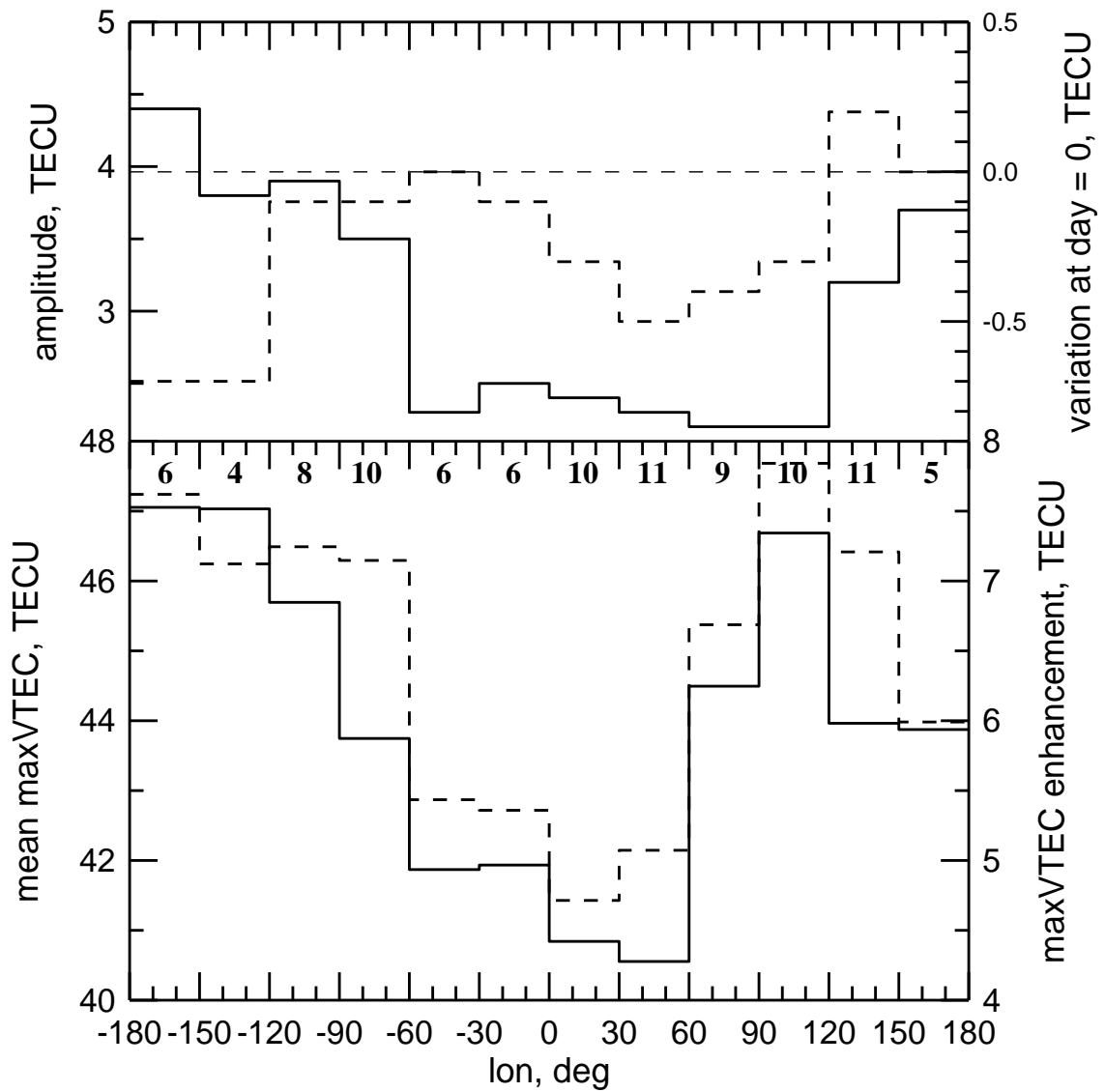


Figure 7. Longitudinal variations of average maxVTEC characteristics during RGSs occurred from 2004 to 2008. Upper panel shows the amplitudes of median maxVTEC variations (solid histogram, left axis) and variation of median maxVTEC during RGS onsets (day = 0) (dashed histogram, right axis). Lower panel shows the mean maxVTEC (solid histogram, left axis) and average enhancements of maxVTEC (dashed histogram, right axis). Bold numbers indicate the amount of receivers in each longitudinal range. The longitudinal range from -60° to 60° is characterized by lowest variability of maxVTEC.

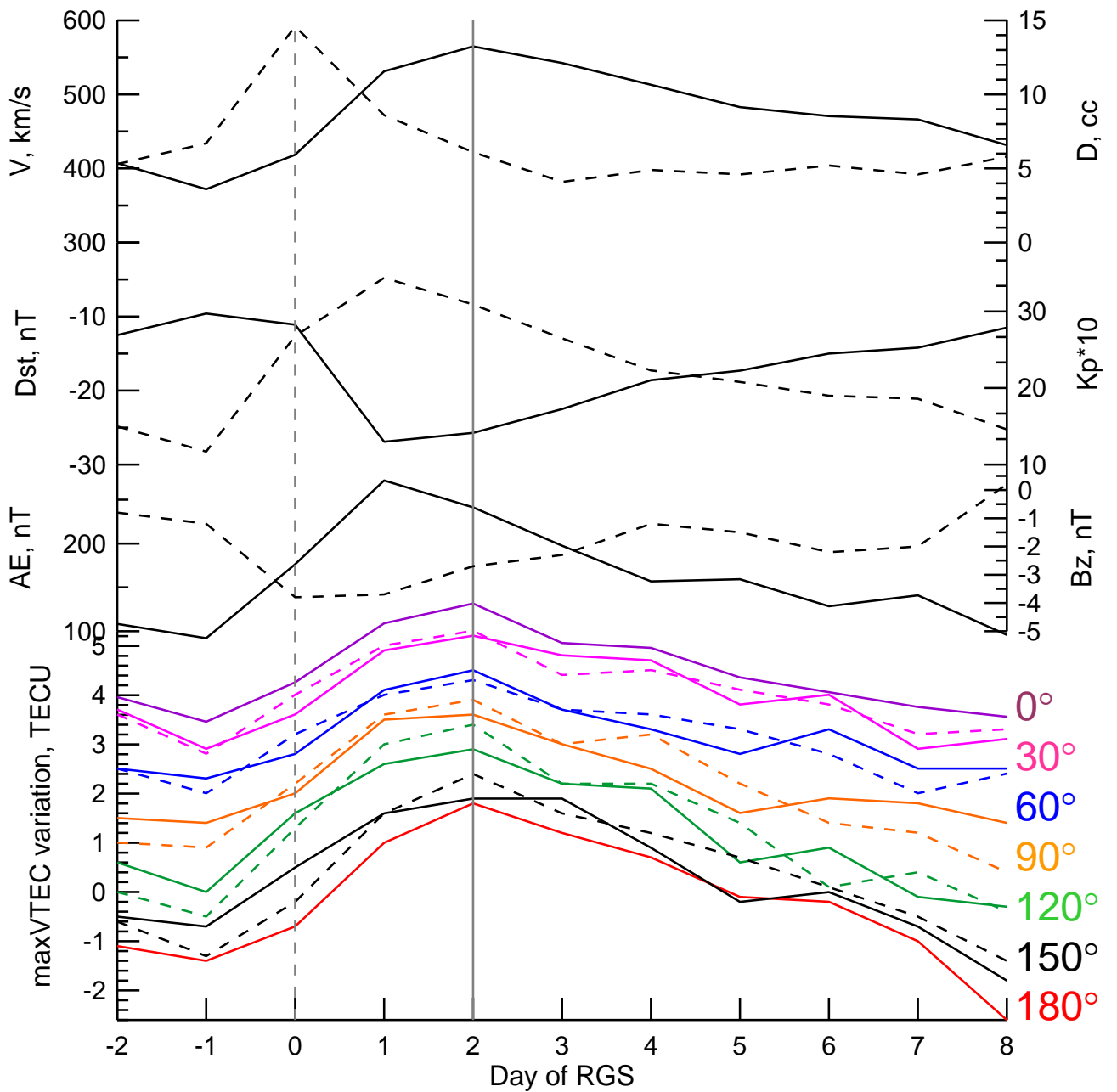


Figure 8. Average variations of various parameters during 185 RGSs occurred from 2004 to 2008 (from top to bottom): maximal solar wind velocity (solid curve, left axis) and density (dashed curve, right axis); minimal Dst (solid curve, left axis) and maximal Kp (dashed curve, right axis); maximal AE (solid curve, left axis) and minimal Bz (dashed curve, right axis); median maxVTEC in various longitudinal ranges (solid and dashed curves correspond to eastern and western longitudes, respectively). The onset of RMS corresponds to the day = 0 (vertical dashed line). Geomagnetic indices peak one day after the onset. Maximum of the solar wind velocity and maxVTEC occur 2 days after the onset (indicated by vertical solid line).

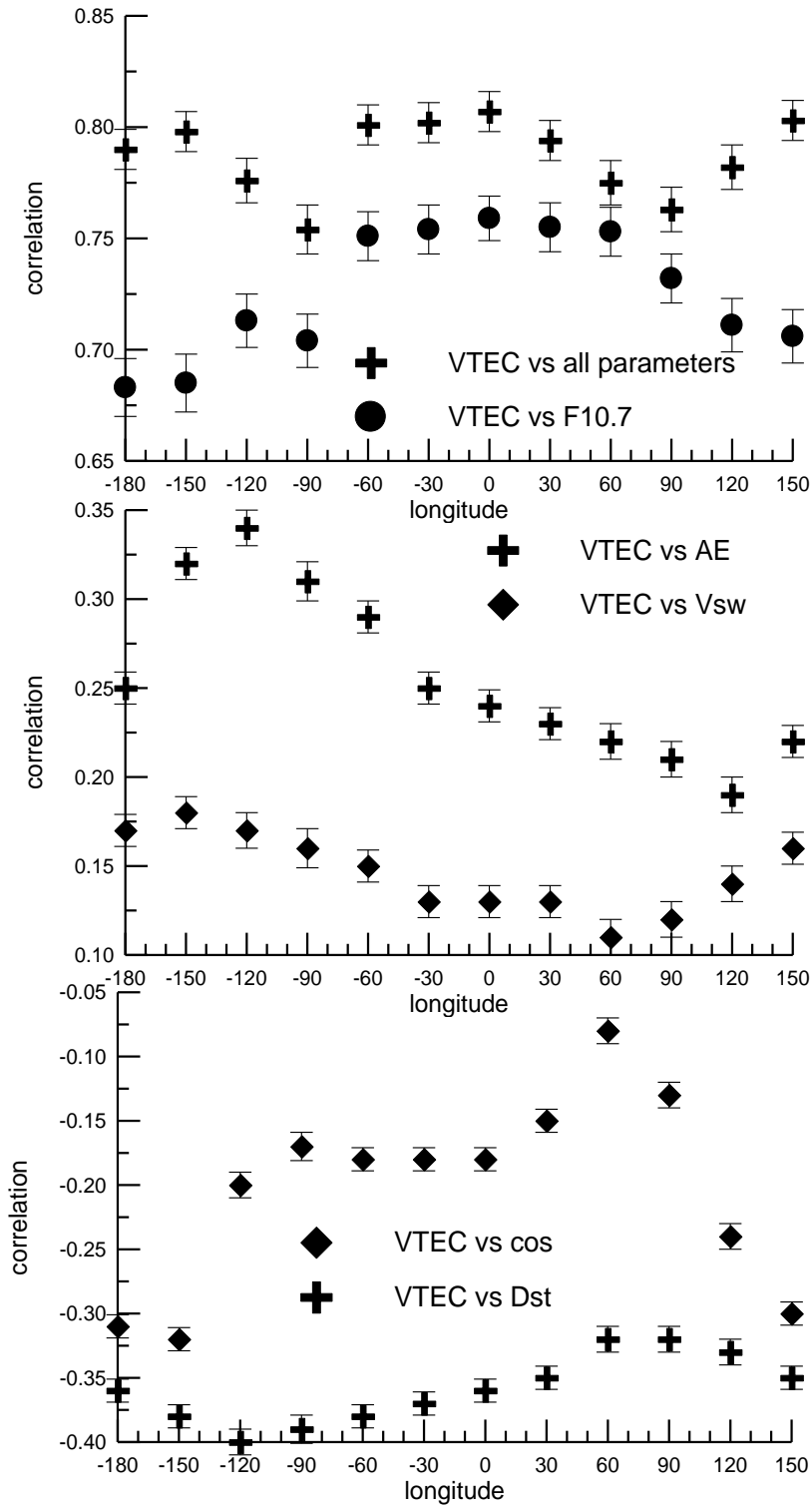
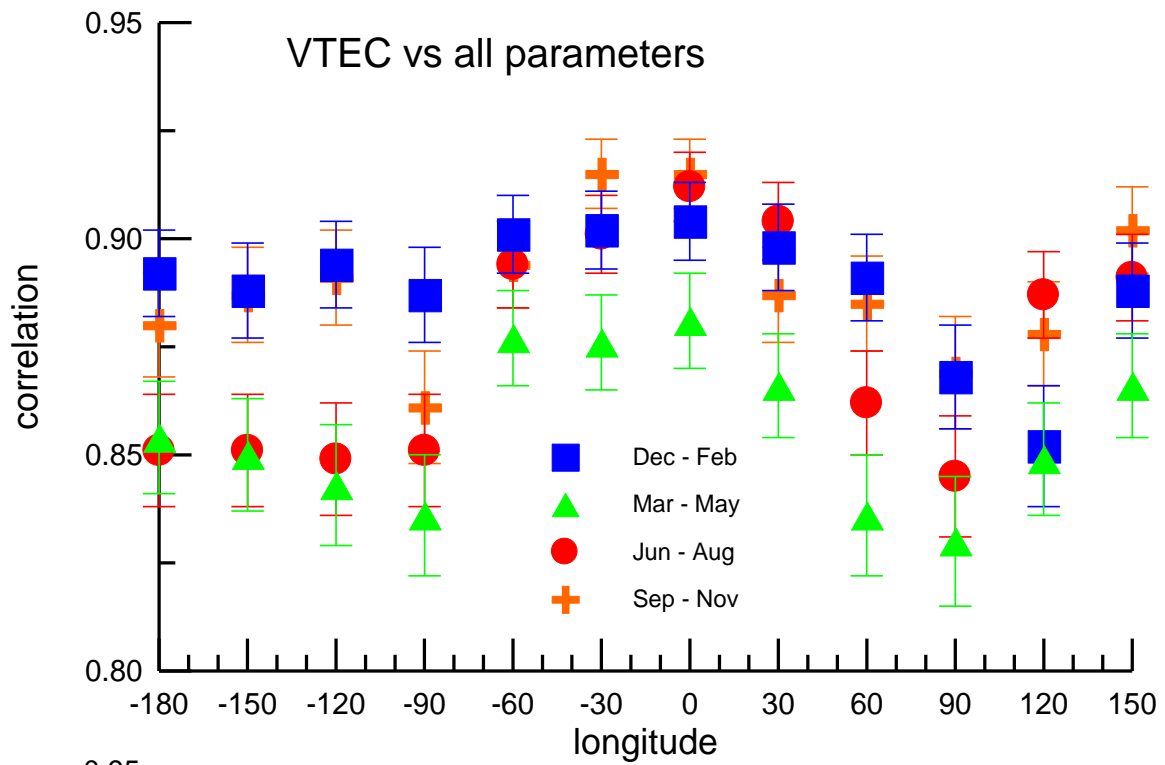
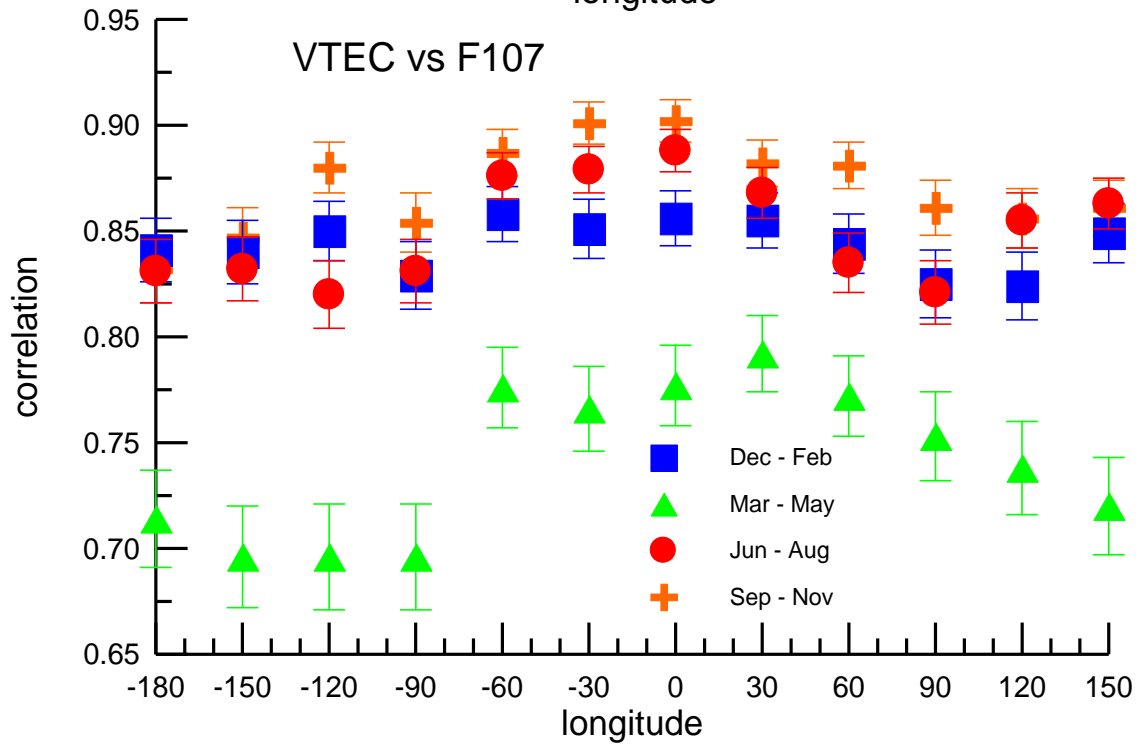


Figure 9. Correlation of maxVTEC with various parameters: (a) all set of parameters and a function of F10.7, (b) AE index and solar wind velocity, (c) Dst index and cosine of annual angle (cos).



a



b

Figure 10. Seasonal variation of the correlation between the maxVTEC and (a) all set of parameters and (b) a function of F10.7. maxVTEC has a weaker correlation with F10.7 during spring equinox at all longitudes.

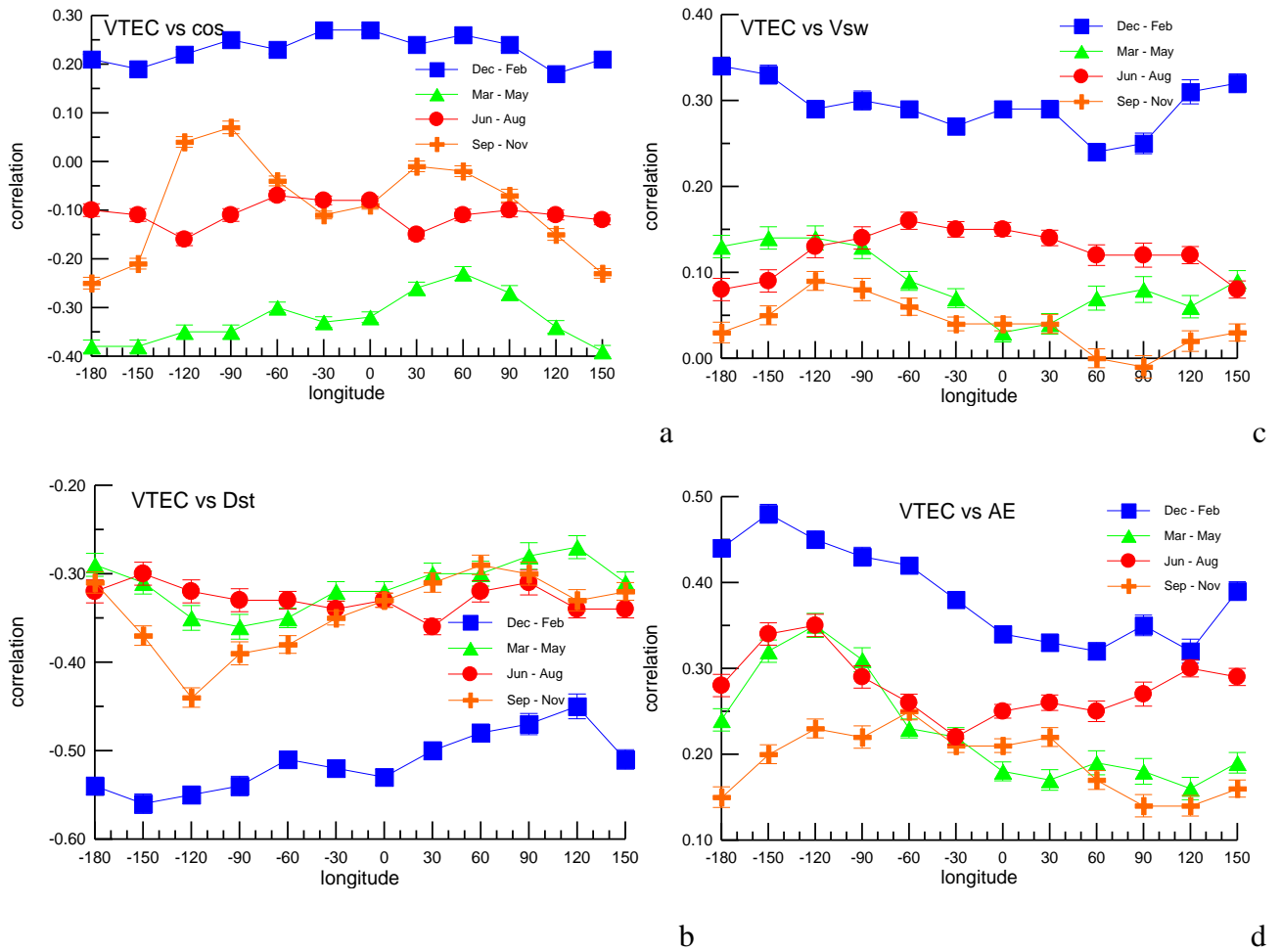
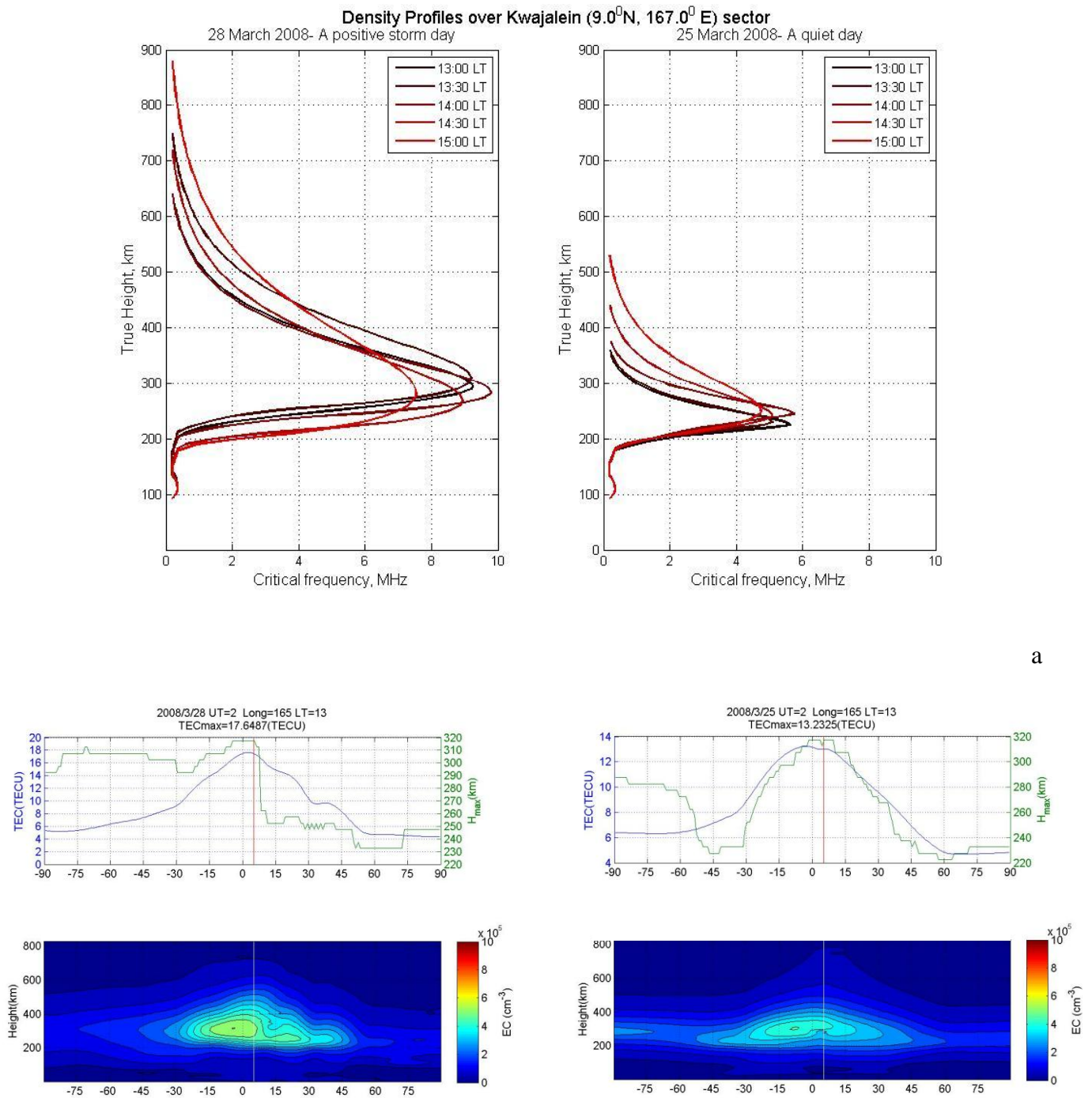


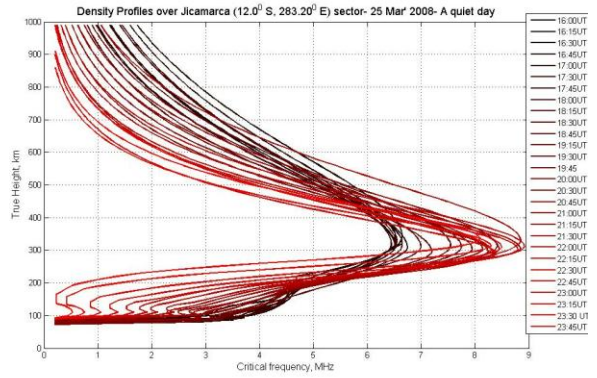
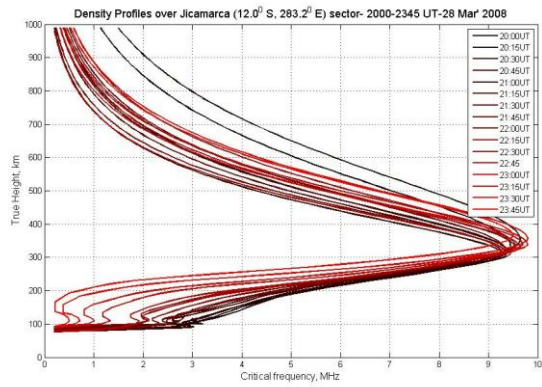
Figure 11. Seasonal variation of the correlation between the maxVTEC and (a) cosine of annual angle, (b) *Dst* index, (c) solar wind velocity, and (d) *AE* index. The cosine of annual angle shows a strong anti-correlation around spring equinox. High correlations with the solar wind and geomagnetic parameters are found during winter (Dec – Feb), especially in the Pacific and South America regions.



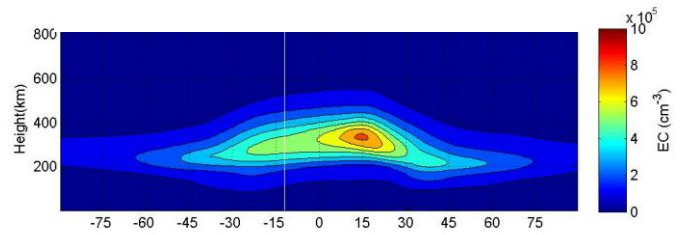
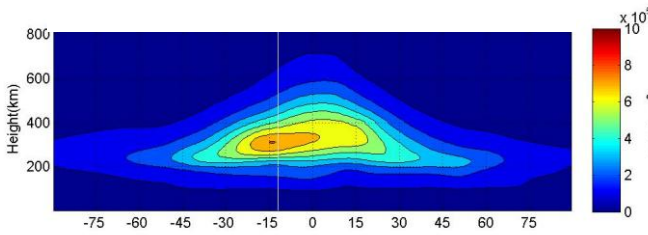
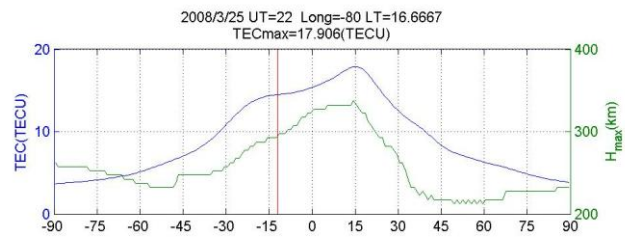
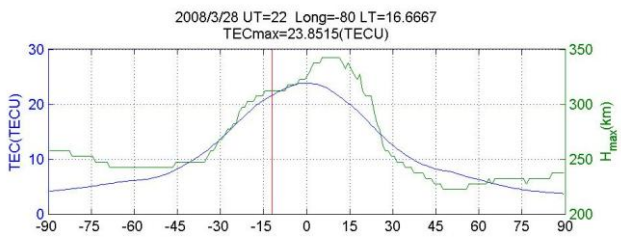
a

b

Figure 12. Height profile of electron content (EC) measured in the Pacific region (a) over Kwajalein (9°N , 167°E) and (b) reconstructed from COSMIC/FORMOSAT-3 radio-occultation tomography at longitude 167°E during a quiet day on 25 March 2008 (right panels) and in the maximum of RGS-related positive ionospheric storm on 28 March 2008 (left panels). During the storm, the EC in the Pacific region increases substantially and the maximum of F-layer elevates up to ~ 50 km from the height of ~ 250 km to ~ 300 km.



a



b

Figure 13. The same as in Figure 12, but over Jicamarca (12°S, 77°W) and at longitude 80°W. During the storm, the EC in the South America region increases substantially and the maximum of F-layer elevates up to ~ 50 km from the height of ~300 km to ~350 km.

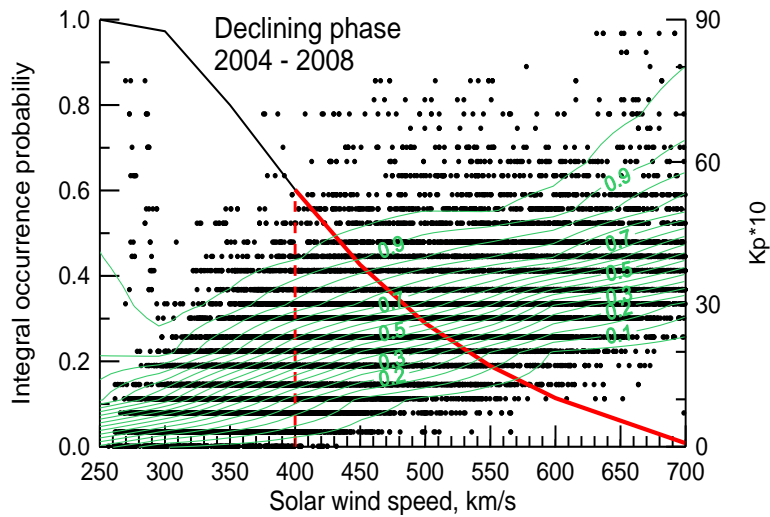


Figure 14. Integral probabilities: (solid curves, left axis) of occurrence of solar wind streams with velocities higher than given and (green isolines with numbers, right axis) of Kp smaller than given at various velocities in 2004 – 2008. Dots depict the scatter plot of Kp versus speed. High-speed solar wind streams with velocity >400 km/s (depicted by red curve) occur in 60% of statistics. More than 30% of statistics is characterized by small $Kp < 3$ under high-speed solar wind streams that is proper for RGSs.